Taylor & Francis
Taylor & Francis Group

RESEARCH PAPER

Check for updates

The role of FYCO1-dependent autophagy in lens fiber cell differentiation

Shahid Y. Khan[a], Muhammad Ali[a], Firoz Kabir[a], Chan Hyun Na[b], Michael Delannoy[c], Yinghong Ma[d], Caihong Qiu[d], M. Joseph Costello[e], J. Fielding Hejtmancik[f], and S. Amer Riazuddin[a]

[a]The Wilmer Eye Institute, Johns Hopkins University School of Medicine, Baltimore, MD, USA; [b]Department of Neurology, Institute for Cell Engineering, Johns Hopkins University School of Medicine, Baltimore, MD, USA; [c]Department of Cell Biology and Imaging Facility, Johns Hopkins University School of Medicine, Baltimore, MD, USA; [d]Yale Stem Cell Center, Yale University School of Medicine, New Haven, CT, USA; [e]Department of Cell Biology and Physiology, University of North Carolina, Chapel Hill, NC, USA; [f]Ophthalmic Genetics and Visual Function Branch, National Eye Institute, National Institutes of Health, Bethesda, MD, USA

ABSTRACT

FYCO1 (FYVE and coiled-coil domain containing 1) is an adaptor protein, expressed ubiquitously and required for microtubule-dependent, plus-end-directed transport of macroautophagic/autophagic vesicles. We have previously shown that loss-of-function mutations in *FYCO1* cause cataracts with no other ocular and/or extra-ocular phenotype. Here, we show *fyco1* homozygous knockout (*fyco1$^{-/-}$*) mice recapitulate the cataract phenotype consistent with a critical role of FYCO1 and autophagy in lens morphogenesis. Transcriptome coupled with proteome and metabolome profiling identified many autophagy-associated genes, proteins, and lipids respectively perturbed in *fyco1$^{-/-}$* mice lenses. Flow cytometry of *FYCO1* (c.2206C>T) knock-in (KI) human lens epithelial cells revealed a decrease in autophagic flux and autophagic vesicles resulting from the loss of FYCO1. Transmission electron microscopy showed cellular organelles accumulated in *FYCO1* (c.2206C>T) KI lens-like organoid structures and in *fyco1$^{-/-}$* mice lenses. In summary, our data confirm the loss of FYCO1 function results in a diminished autophagic flux, impaired organelle removal, and cataractogenesis.

Abbreviations: CC: congenital cataracts; DE: differentially expressed; ER: endoplasmic reticulum; FYCO1: FYVE and coiled-coil domain containing 1; hESC: human embryonic stem cell; KI: knock-in; OFZ: organelle-free zone; qRT-PCR: quantitative real-time PCR; PE: phosphatidylethanolamine; RNA-Seq: RNA sequencing; SD: standard deviation; sgRNA: single guide RNA; shRNA: shorthairpin RNA; TEM: transmission electron microscopy; WT: wild type

Introduction

The ocular lens is an excellent tissue to investigate intricate details of development. The lens develops from the head ectoderm that thickens to form the lens placode and invaginates together with the optic vesicle to form the lens pit [1,2]. The lens pit separates from the ectoderm to form the lens vesicle that gives rise to anterior and posterior single layers of cells [1,2]. The cells of the anterior layer differentiate into the epithelium while cells forming the posterior layer differentiate into primary fiber cells forming the lens nucleus [1,2].

The lens epithelial cells at the anterior pole differentiate into fiber cells at the transition zones [2]. The lens fiber cells are generated throughout life from lens epithelial cells that elongate and differentiate into secondary fiber cells [2]. During differentiation, the lens fiber cells degrade their cellular organelles (hereafter referred to as organelles) through multiple processes [3,4], to create the organelle-free zone (OFZ), which is critical for the transparency and the physiological functioning of the lens.

Disruption of the processes during lens fiber cell differentiation can lead to persistent organelles in lens fiber cells that impede creation of the OFZ ultimately resulting in the development of cataracts [5–7], the leading cause of blindness worldwide. Cataract is a clouding or opacity of an otherwise transparent lens of the eye. It interferes with the focusing of the incoming light on the retina, and if left untreated during infancy, it can affect visual development eventually leading to blindness [8].

Macroautophagy/autophagy is an important cellular mechanism responsible for the recycling of damaged organelles and protein aggregates in many tissues [9]. The role of autophagy during lens fiber cell differentiation is still controversial since organelles are not retained in lens fiber cells of lens-specific *atg5* knockout mice [10,11]. However, multiple studies have reported the expression of autophagy-associated genes in the lens [12,13] and autophagosomes are detected in lens epithelial cells, and differentiating lens fiber cells [14,15].

The FYVE zinc finger domain is named after the four cysteine-rich proteins: Fab1 (yeast ortholog of PIKfyve), YOTB, Vac1 (vesicle transport protein), and EEA1 [16]. FYCO1 (FYVE and coiled-coil domain containing 1) is an adaptor protein required for microtubule-dependent, plus-end-directed transport of autophagic vesicles, delivering autophagosomes to the lysosomes for degradation [17,18]. We

---

have previously shown that loss-of-function mutations in *FYCO1* cause cataracts [19,20].

Here, we recapitulated the cataract phenotype in *fyco1* knockout mice and examined the loss of FYCO1 function in multiple *in vitro* and *in vivo* experimental systems as means of exploring the physiological significance of FYCO1 in lens morphogenesis. Our results confirm an essential role of FYCO1-dependent autophagy in lens fiber cell differentiation where the loss of FYCO1 function results in diminished autophagic flux, impaired organelle removal, and cataractogenesis.

Results

fyco1 *homozygous knockout* (fyco1$^{-/-}$) *mice develop bilateral cataracts*

We previously reported multiple families with loss-of-function mutations in *FYCO1* responsible for autosomal recessive congenital cataracts (arCC) with no other ocular and/or extra-ocular anomalies [19,20]. Taken together, mutations identified in *FYCO1* contribute nearly 15% of the total genetic load of cataractogenesis in our cohort of Pakistani families with arCC.

We developed *fyco1*$^{-/-}$ mice to investigate the physiological significance of FYCO1 in lens morphogenesis in a system that closely mimics the human eye. The quantitative real-time PCR (qRT-PCR) identified only residual expression of *Fyco1* in *fyco1*$^{-/-}$ mice lenses (Fig. S1A). We performed a detailed phenotypic assessment of *fyco1*$^{-/-}$ mice lenses (Figure 1A-D). The *fyco1*$^{-/-}$ mice exhibited initial signs of lens opacities at four weeks that developed into mild cataracts around eight weeks and mature cataracts by 16 weeks of age (Figure 1A, C). While the extent of the lens opacities varied among *fyco1*$^{-/-}$ mice, both *EIIa*-Cre-mediated *fyco1*$^{-/-}$ and *Prm1*-Cre-mediated *fyco1*$^{-/-}$ mice developed cataracts, bilaterally. No cataracts were detected in *Fyco1* heterozygous knockout (*Fyco1*$^{+/-}$) mice (Figure 1B, D), or *Fyco1* LoxP floxed (*Fyco1*$^{+/+}$) mice (Fig. S1B).
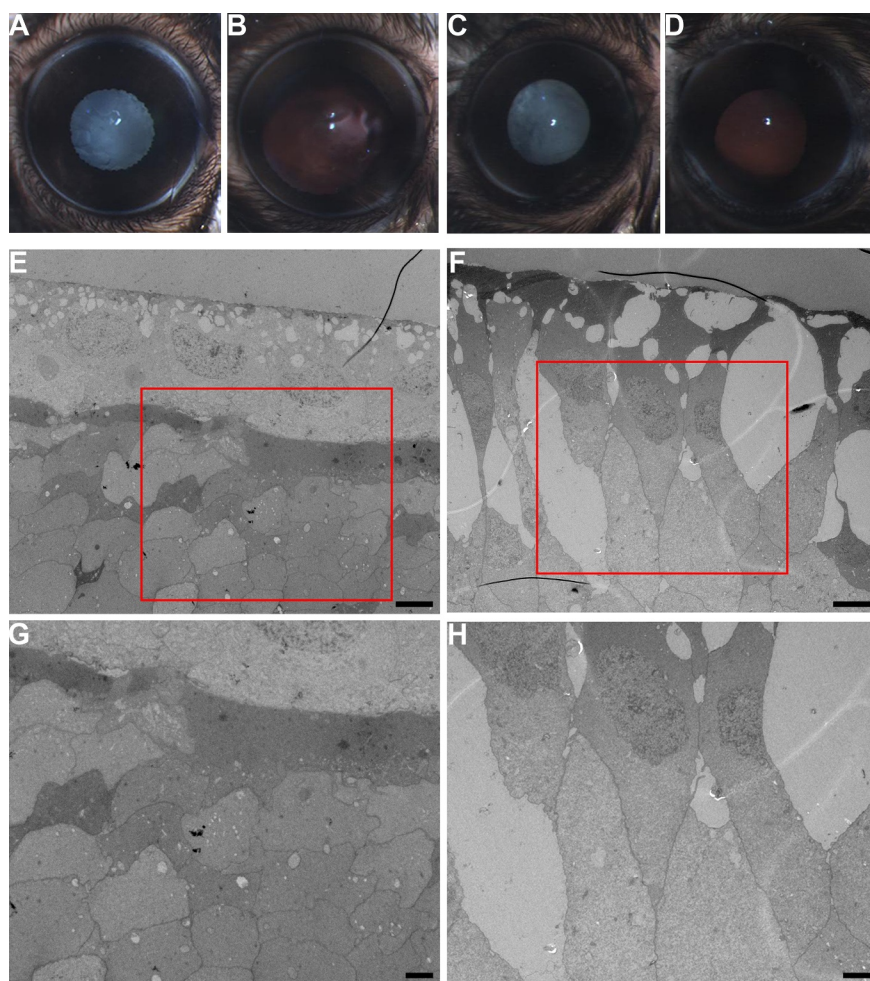

Figure 1. Phenotypic assessment of *fyco1* homozygous knockout (*fyco1*$^{-/-}$) mice lenses revealed bilateral cataracts and abnormal morphology of lens epithelial and fiber cells. (A–D) Assessment of lens opacities in the knockout mice lenses. The examination identified cataracts in (A) 16-weeks old *EIIa*-Cre-mediated *fyco1*$^{-/-}$ and (C) 16-weeks old *Prm1*-Cre-mediated *fyco1*$^{-/-}$ mice lenses. No cataracts were observed in age-matched (B) *EIIa*-Cre-mediated *fyco1*$^{+/-}$ and (D) *Prm1*-Cre-mediated *fyco1*$^{+/-}$. (E–H) Transmission electron microscopy (TEM) of wild type (WT) and *fyco1*$^{-/-}$ mouse lens at postnatal day 60 (P60). The analysis of WT mouse lens revealed a normal morphology of lens epithelial and fiber cells (E, G). In contrast, *fyco1*$^{-/-}$ mouse lens epithelial cells show extensive vacuolization while fiber cells are large and exhibit irregular shapes (F, H). Note: Image magnifications: 1,850x (E, F), and 3,400x (G, H); Scale bars: 5 µm (E, F), and 2 µm (G, H). Panels G and H are enlarged images of the boxed areas in panels E and F, respectively.

Transmission electron microscopy (TEM) was performed on postnatal day 60 (P60) wild type (WT) and *fyco1*⁻/⁻ mice lenses (Figure 1E-H). Electron micrographs of WT mice revealed normal morphology of lens epithelial and fiber cells (Figure 1E, G) while age-matched *fyco1*⁻/⁻ mice lens epithelial and fiber cells show extensive vacuolization and irregular shape (Figure 1F, H).

Transcriptome profiling identified differentially expressed (DE) genes in fyco1⁻/⁻ *mice lenses*

We first examined the transcriptome profile of P0 WT and *fyco1*⁻/⁻ mice lenses to identify DE genes resulting from the loss of FYCO1. Since the first signs of cataracts appear around four weeks in *fyco1*⁻/⁻ mice, we used P0 mice lenses for OMIC (transcriptome, proteome, and metabolome) profiling to separate cause (loss of FYCO1) and effect (cataractogenesis), which otherwise, would have complicated the downstream analysis. RNA sequencing (RNA-Seq) detected expression of 10,442 and 10,296 genes (≥1.0 FPKM, fragments per kilobase of transcript per million) in the WT and *fyco1*⁻/⁻ P0 mice lenses, respectively (Table S1). A comparative analysis of genes expressed in the mice lenses identified 2,665 DE ($p < 0.05$) genes including 1,415 with elevated expression and 1,250 with lower transcript counts in *fyco1*⁻/⁻ mice lenses compared with WT mice lenses (Table S1).

Among DE genes, *Bfsp1, Gja3, Tdrd7, Hsf4,* and *Gja1* showed higher expression in *fyco1*⁻/⁻ mice lenses (Table S1). Furthermore, we identified elevated expression of *Capn3, Caprin2,* and *Casp7* in *fyco1*⁻/⁻ mice lenses (Table S1). Multiple autophagy-associated genes showed higher expression in *fyco1*⁻/⁻ mice lenses including *Atg101, Atg3, Atg9a, Becn1, Lamp2,* and *Sqstm1/p62* (Table S1). Finally, *Bfsp2, Pax6,* and *Pxdn* exhibited lower transcript counts in *fyco1*⁻/⁻ mice lenses (Table S1).

Proteome profiling identified differential abundance or deficiency of proteins in fyco1⁻/⁻ *mice lenses*

We next examined the proteome profile of P0 WT and *fyco1*⁻/⁻ mice lenses to identify differential abundance or deficiency of proteins resulting from the loss of FYCO1. A threshold of >2 standard deviation (SD) was set to establish differential protein abundance or deficiency, which yielded 160 proteins, including 19 exhibiting abundance and 141 with diminished quantities in *fyco1*⁻/⁻ mice lenses compared with WT mice lenses (Table S2). BFSP1, BFSP2, GJA3, MIP, BIRC7, TDRD7, and HSF4 exhibited abundance in *fyco1*⁻/⁻ mice lenses (Table S2). In contrast, diminished counts of GJA1, PAX6, and PXDN were identified in *fyco1*⁻/⁻ mice lenses (Table S2).

Importantly, multiple autophagy-associated proteins including ATG7, ATG12, SQSTM1/p62, WIPI2, and BAG3 exhibited abundance in *fyco1*⁻/⁻ mice lenses while LAMP2 levels were diminished in *fyco1*⁻/⁻ mice lenses compared to WT mice lenses (Table S2). We also identified differential abundance or deficiency of many proteases including CAPN3, CAPRIN2, and CASP7 accumulated and CAPRIN1 diminished in *fyco1*⁻/⁻ mice lenses (Table S2). It should be noted that CAPN3, a calcium-dependent, non-lysosomal

cysteine calpain protease exhibited a 1.81-fold abundance in *fyco1*⁻/⁻ mice lenses (Table S2).

Among the autophagy-associated proteins accumulated in *fyco1*⁻/⁻ mice lens proteome was SQSTM1/p62 (Figure 2A) exhibiting a 1.61-fold higher level (Figure 2B). Importantly, SQSTM1/p62 exhibited increased levels in both transcriptome and proteome analyses of P0 *fyco1*⁻/⁻ mice lenses (Tables S1-2). It is noteworthy that the concentration of SQSTM1/p62 inversely correlates with autophagic flux i.e., higher levels of SQSTM1/p62 suggest a decrease in autophagic flux. To further validate the levels of SQSTM1/p62, we performed Western blot that revealed a 1.48-fold higher level of SQSTM1/p62 in *fyco1*⁻/⁻ mice lenses (Figure 2C–D) suggesting that loss of FYCO1 results in diminished autophagy in the mice lenses.

Metabolome profiling identified elevated levels of phosphatidylethanolamine (PE)- associated metabolites in fyco1⁻/⁻ *mice lenses*

FYCO1 has been implicated in autophagosome trafficking through binding to the PE-lipidated form of MAP1LC3B (microtubule-associated protein 1 light chain 3 beta), LC3B-II, critical for the formation of autophagosomes [17,18]. Since the loss of FYCO1 results in diminished autophagy in *fyco1*⁻/⁻ mice lenses, we reasoned that a relatively lower number of autophagosomes will be degraded in autolysosomes, which in turn, would result in a modest accumulation of PE or PE-associated metabolites in *fyco1*⁻/⁻ mice lenses. We, therefore, examined the metabolome profile of P0 WT and *fyco1*⁻/⁻ mice lenses.

The metabolome profiling identified 353 metabolites in the P0 mice lenses (Table S3). Of these, 75 metabolites exhibited differential counts ($p < 0.05$), including 66 exhibiting abundance and nine with diminished quantities in *fyco1*⁻/⁻ mice lenses compared with WT mice lenses (Table S3). We identified 13 PE-associated metabolites, PE phospholipids having the same base structure but different acyl chains. Among these, 12 PE metabolites exhibited elevated levels including six metabolites exhibiting significantly ($p < 0.05$) higher levels in *fyco1*⁻/⁻ mice lenses compared with WT mice lenses (Table S3).

PE is the second-most abundant phospholipid in mammalian membranes and can be generated through four different enzymatic pathways [21]. While we only focused on the PE phospholipids, the data suggest that the absence of FYCO1 is responsible for a modest accumulation of PE phospholipids, in line with the notion of diminished autophagy suggested by elevated levels of SQSTM1/p62 in the transcriptome and proteome datasets. Taken together, the OMIC datasets strongly suggest that the loss of FYCO1 function results in diminished autophagic flux in *fyco1*⁻/⁻ mice lenses.

Multiphoton laser scanning microscopy validated a decrease in autophagic flux in fyco1⁻/⁻ *mice lenses*

To further examine the loss of FYCO1 dependent decrease in autophagic flux in *fyco1*⁻/⁻ mice lenses, we took advantage of commercially available *CAG-RFP-EGFP-Map1lc3b* mice. We
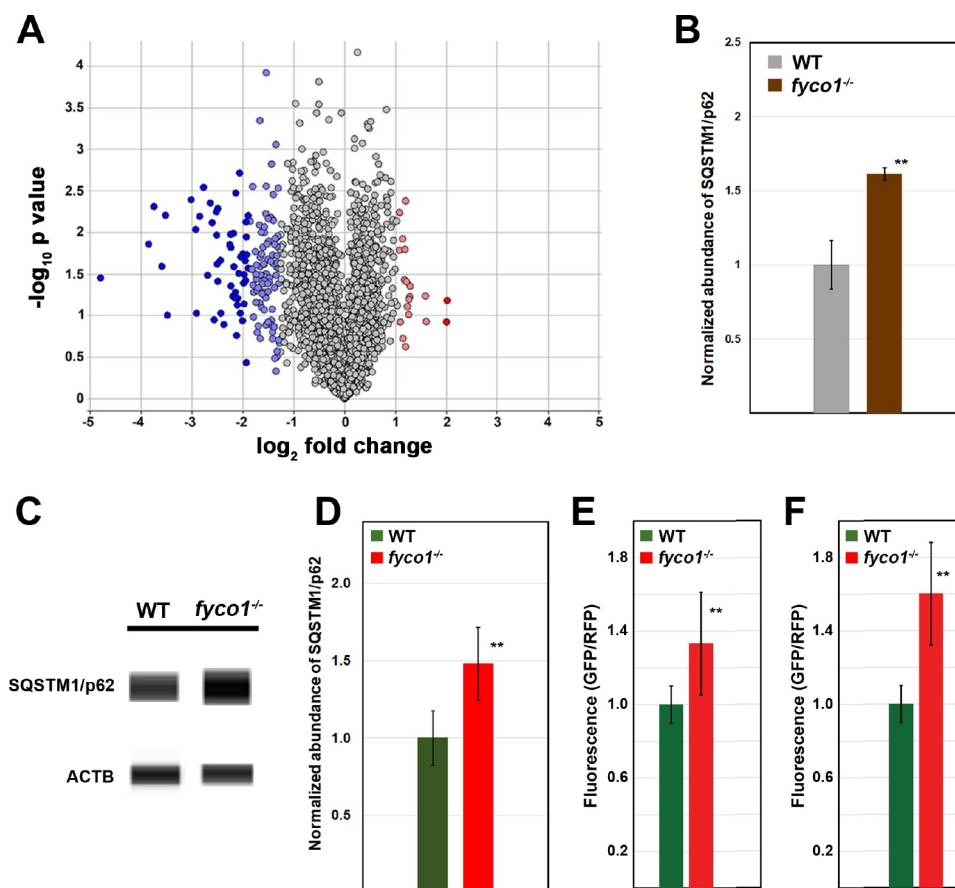
Figure 2. Functional assessment of *fyco1* homozygous knockout (*fyco1*$^{-/-}$) mice lenses revealed impaired autophagy. (A) Volcano plot illustrating the differential abundance or deficiency of proteins in *fyco1*$^{-/-}$ mice lenses at postnatal day 0 (P0). A comparative analysis identified 160 proteins (>2 standard deviation (SD)) including 19 proteins exhibiting abundance and 141 with diminished quantities in *fyco1*$^{-/-}$ mice lenses compared to wild type (WT) mice lenses. Proteins exhibiting abundance are shown in light red (SD > 2) and dark red (SD ≥ 6), and diminished counts are shown in light blue (SD > -2) and dark blue (SD ≥ -6) in *fyco1*$^{-/-}$ mice lenses. Note: the fold change is represented in $\log_2$ scale, depicted on the x-axis and the statistical significance is represented in $-\log_{10}$ scale, depicted on the y-axis. The use of $-\log_{10}$ values means that proteins having greater statistical significance are higher in the plot. (B) The proteome analysis detected a 1.61-fold higher concentration of SQSTM1/p62 in *fyco1*$^{-/-}$ mice lenses at P0 compared to age-matched WT mice lenses. Asterisks: $p < 0.05$. (C) Capillary electrophoresis-based Western blot analysis revealed an accumulation of SQSTM1/p62 in *fyco1*$^{-/-}$ mice lenses at P0. (D) Quantification of Western blot revealed 1.48-fold higher levels of SQSTM1/p62 in *fyco1*$^{-/-}$ mice lenses at P0 compared to age-matched WT mice lenses. The SQSTM1/p62 levels were normalized against ACTB/β-Actin. Asterisks: $p < 0.05$. (E,F) Multiphoton laser-scanning microscopy was performed on *CAG-RFP-GFP-Map1lc3b* WT and *CAG-RFP-GFP-Map1lc3b-fyco1*$^{-/-}$ mice lenses. The analysis revealed (E) 1.3- and (F) 1.6-fold higher GFP intensity in the whole lens and the anterior lens including lens epithelium, respectively. Asterisks: $p < 0.05$.

crossed *fyco1*$^{-/-}$ mice with *CAG-RFP-EGFP-Map1lc3b* transgenic mice. The progeny of this cross was bred to homozygosity to generate *CAG-RFP-EGFP-Map1lc3b-fyco1*$^{-/-}$ mice. The autophagic flux in *CAG-RFP-EGFP-Map1lc3b-fyco1*$^{-/-}$ mice lenses were examined using the sensitivity of GFP fluorescence i.e., quenching in an acidic environment of lysosomes or autolysosomes. To eliminate concerns that the intrinsic fluorescence of the retina might interfere with the analysis of the lens, an *ex-vivo* strategy was adopted to measure RFP and GFP fluorescence intensities.

The mice eyes were enucleated, WT and *fyco1*$^{-/-}$ mice lenses expressing RFP-EGFP-MAP1LC3B were isolated, fixed in 3.7% paraformaldehyde, and RFP and GFP fluorescence intensities were measured in 10 μm Z-stacks using a multiphoton laser scanning microscope (Fig. S1C-D). Analysis of *fyco1*$^{-/-}$ mice lenses revealed a 1.3- and 1.6-fold higher GFP fluorescence intensity ($p < 0.05$) in the whole lens and the anterior lens including lens epithelium, respectively (Figure 2E–F). These results validated the findings of OMIC profiling experiments of diminished autophagic flux in *fyco1*$^{-/-}$

mice lenses. It is worth noting that 1.3- and 1.6-fold increase in GFP fluorescence, while statistically significant, is modest overall, and is consistent with the notion that loss of FYCO1 results in diminished autophagy rather than an overall ablation of autophagy.

Diminished autophagic flux in FYCO1 (c.2206C>T) knock-in (KI) human lens epithelial (HLE) cells

To further investigate the loss of FYCO1-dependent decrease in autophagic flux, we engineered HLE cells harboring a cataract causing mutation in *FYCO1* (c.2206C>T; p.Q736*) that has been identified in multiple individuals with congenital cataracts [19]. HLE-B3 cells were transfected with a single guide RNA (gRNA) and a donor DNA homozygous for the mutation in *FYCO1* (c.2206C>T). The successful targeting of the *FYCO1* (c.2206C>T) allele was confirmed through bi-directional Sanger sequencing (Fig. S2A). The qRT-PCR revealed only residual expression of *FYCO1* mRNA in the KI HLE cells while the short-hairpin

RNA (shRNA)-mediated silencing of *FYCO1* reduced endogenous expression of *FYCO1* mRNA in WT HLE cells by about 60% (p < 0.05) (Fig. S2B). The CRISPR-Cas9-engineered HLE cells harboring the *FYCO1* (c.2206C>T) allele were used in multiple assays to investigate the effect of the loss of FYCO1 and hereafter referred to as *FYCO1* KI HLE cells.

First, we investigated the endogenous level of SQSTM1/p62 in *FYCO1* KI HLE cells. The flow cytometry-based quantification identified an accumulation of cellular SQSTM1/p62 (p < 0.0005) in *FYCO1* KI HLE cells (Figure 3A), in agreement with the accumulation of SQSTM1/p62 in *fyco1*$^{-/-}$ mice lenses (Figure 2A–D) and providing further evidence of a decrease in autophagy resulting from the loss of FYCO1.

Second, we used tandem fluorescently tagged MAP1LC3B to monitor autophagic flux in *FYCO1* KI HLE cells. We transfected WT and *FYCO1* KI HLE cells with a mRFP-GFP-LC3 plasmid followed by treatment with rapamycin and two lysosomal protease inhibitors (E64d and pepstatin A). The mean relative fluorescence intensity of GFP and RFP was analyzed by flow cytometry that revealed a 1.87-fold higher green-to-red fluorescence ratio (p < 0.05) in *FYCO1* KI HLE cells compared with WT HLE cells (Figure 3B). These findings are consistent with the higher GFP fluorescence intensity identified in the *CAG-RFP-EGFP-Map1lc3b-fyco1*$^{-/-}$ mice lenses (Figure 2E–F).

Third, we investigated LC3B-II in *FYCO1* KI HLE cells using flow cytometry-based quantification. Upon induction of autophagy, LC3B-I is converted to a membrane-bound
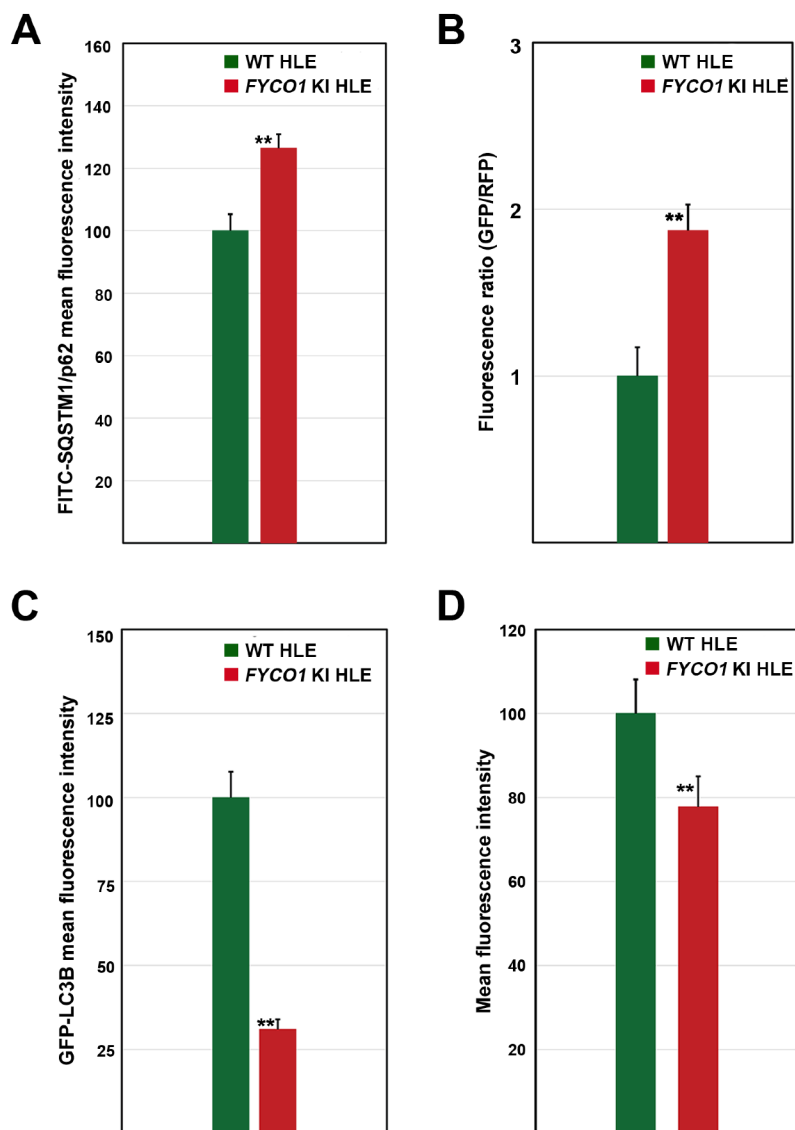

Figure 3. Functional analysis of *FYCO1* (c.2206C>T) knock-in (KI) human lens epithelial (HLE) cells revealed impaired autophagy. (A) Flow cytometry-based quantification of endogenous SQSTM1/p62 in *FYCO1* KI HLE cells. The analysis revealed accumulation of SQSTM1/p62 in *FYCO1* KI HLE cells compared to wild type (WT) cells. Asterisks: p < 0.0005. (B) Flow cytometry-based quantification of autophagic flux in *FYCO1* KI HLE cells using a tandem fluorescent-tagged LC3B plasmid (mRFP-GFP-LC3). The analysis revealed a higher GFP to RFP ratio in *FYCO1* KI HLE cells compared to WT cells. Asterisk: p < 0.05. (C) Flow cytometry-based quantification of exogenously expressed GFP labeled LC3B in *FYCO1* KI HLE cells. The analysis revealed a 69% reduced GFP fluorescence intensity in *FYCO1* KI HLE cells compared with WT HLE cells. Asterisks: p = 9.068e^{-12}. (D) Flow cytometry-based quantification of CYTO-ID labeled autophagic vesicles in *FYCO1* KI HLE cells. The analysis revealed a reduced green fluorescence intensity in *FYCO1* KI HLE cells compared with WT HLE cells. Asterisks: p = 3.475e^{-5}.

lipidated form (LC3B-II) that is sequestered into autophagosome membranes, and therefore the membrane-bound LC3B-II can be used to estimate the autophagic flux [22,23]. We transfected WT and *FYCO1* KI HLE cells with the EGFP-LC3B plasmid followed by treatment with chloroquine for 4 h to block the autophagic flux. The WT and *FYCO1* KI HLE cells were harvested 24-h post-transfection and briefly treated with saponin to allow the non-membrane-bound, EGFP-LC3B-I to leave the cells through pores in the cell membrane while the membrane-bound, EGFP-LC3B-II remained within the HLE cells. The levels of bound EGFP were estimated by flow cytometry [23]. The analysis identified a 69% decrease in EGFP-LC3B-II fluorescence signal (p = $9.068e^{-12}$) in *FYCO1* KI HLE cells compared to WT HLE cells (Figure 3C) suggesting a decrease in autophagic flux in *FYCO1* KI HLE cells.

Fourth, we examined the overall count of autophagic vesicles in *FYCO1* KI HLE cells using CYTO-ID, an autophagy detection dye that preferably stains autophagic vacuoles in live cells. WT and *FYCO1* KI HLE cells were treated with chloroquine for 4 h followed by staining with CYTO-ID and analyzed by flow cytometry. Flow cytometry-based quantification of chloroquine-treated, CYTO-ID-stained cells revealed a 22% reduction in the signal (p = $3.475e^{-5}$) in *FYCO1* KI HLE cells compared to WT HLE cells (Figure 3D) suggesting a decrease in autophagic flux in *FYCO1* KI HLE cells.

Taken together, analyses of *FYCO1* KI HLE cells show accumulation of SQSTM1/p62, pH-sensitive spatial localization of fluorescent-tagged-LC3 in the cytoplasm, a saponin-treatment dependent decrease in EGFP-LC3B-II signal, and reduction in the CYTO-ID-stained autophagic vacuoles, all confirming a decrease in autophagic flux resulting from the loss of FYCO1 consistent with the OMIC profiling and *in vivo* analysis of *fyco1⁻/⁻* mice lenses.

Opaque central zones in FYCO1 (c.2206C>T) KI human embryonic stem cell (hESC)-derived lentoid bodies

While cultured lens epithelial cells provide an excellent system to investigate many characteristics of lens-associated genes and proteins, it is a static system in which the lens epithelial cells do not differentiate into fiber cells. Therefore, we sought a dynamic system to investigate the impact of the loss of FYCO1 function and a decrease in autophagy on lens fiber cell differentiation. We exploited the inherent property of pluripotent stem cells to differentiate into many kinds of cells in the human body including lens-like organoid structures termed lentoid bodies. We first engineered hESCs by introducing a cataract causing mutation in *FYCO1* (c.2206C>T; p.Q736*) through a method similar to the one adopted for developing the *FYCO1* KI HLE cells. The successful targeting of *FYCO1* (c.2206C>T) allele was confirmed through bi-directional Sanger sequencing and qRT-PCR revealed residual levels of *FYCO1* mRNA in *FYCO1* KI hESCs (Fig. S2C-D). The CRISPR-Cas9-engineered hESCs harboring the *FYCO1* (c.2206C>T) allele were differentiated to lentoid bodies to investigate the effect of the loss of FYCO1 and hereafter referred to as *FYCO1* KI hESCs.

We adopted the "fried-egg" method that was published initially by Fu et al [24] and later by Ali et al [25,26] with a few modifications. On differentiation day 6, epithelial-like lens-fated cells present at the periphery of both WT and *FYCO1* KI hESC colonies were isolated and transferred into a new Matrigel-coated plate (Fig. S3A). The fried egg-like differentiated colonies started to appear around differentiation day 8 in both the WT and *FYCO1* KI hESCs that transformed into compact structures by day 11 (Fig. S3A). Up till day 11, no morphological differences were observed between WT and *FYCO1* KI hESC-derived presumptive lentoid bodies. The effect of the KI allele started to become apparent around differentiation day 25 and become more evident on day 35 with opaque zones present in the *FYCO1* KI hESC-derived lentoid bodies, in sharp contrast to the WT hESC-derived lentoid bodies that displayed extensive transparent zones (Figure 4). We reasoned that the opaque zones in *FYCO1* KI hESC-derived lentoid bodies are due to the loss of FYCO1 function and therefore, we next asked if the loss of FYCO1 function results in diminished autophagy in differentiating lentoid bodies.

Accumulation of SQSTM1/p62 in FYCO1 *KI hESC-derived lentoid bodies*

We next performed a comparative proteome analysis of WT and *FYCO1* KI hESC-derived lentoid bodies on differentiation day 25 to identify differential abundance or deficiency of proteins in the *FYCO1* KI lentoid bodies. A threshold of >2 SD was set to establish differential protein abundance or deficiency, which yielded 311 proteins including 170 exhibiting abundance and 141 with diminished quantities in *FYCO1* KI hESC-derived lentoid bodies compared to WT hESC-derived lentoid bodies (Fig. S3B-C and Table S4). Among the proteins exhibiting differential abundance, we identified accumulation of SQSTM1/p62 in *FYCO1* KI hESC-derived lentoid bodies (Fig. S3B and Table S4), consistent with the results of proteome profiling of *fyco1⁻/⁻* mice lenses (Figure 2B), Western blot analysis of *fyco1⁻/⁻* mice lenses (Figure 2D), and flow cytometry-based analysis of *FYCO1* KI HLE cells (Figure 3A). Accumulation of SQSTM1/p62 in *FYCO1* KI hESC-derived lentoid bodies further established a decrease in autophagy resulting from the loss of FYCO1.

TEM reveals retention of organelles in FYCO1 *KI hESC-derived lentoid bodies*

To determine the effect of the loss of FYCO1 dependent decrease in autophagy on the removal of organelles during differentiation of hESCs to lentoid bodies, we performed TEM on WT and *FYCO1* KI hESC-derived lentoid bodies on differentiation day 25. Fu et al have reported a comprehensive characterization of lentoid bodies identifying lens epithelial-like cells and lens fiber-like cells in lentoid bodies [24]. The ultrastructural analysis of WT and *FYCO1* KI hESC-derived lentoid bodies on differentiation day 25 revealed a mixture of lens epithelial-like cells (Figure 5) near the periphery and
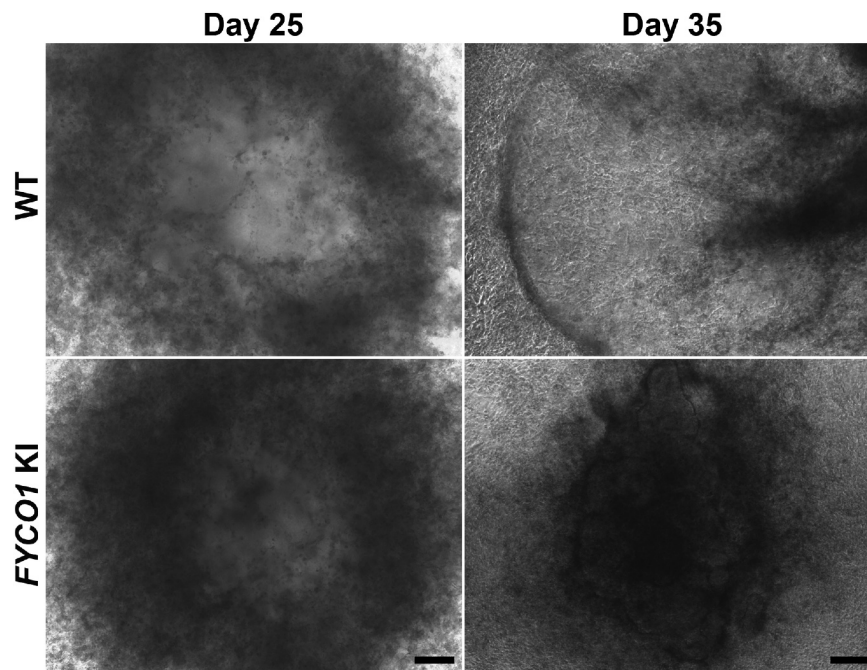
Day 25   **Day 35**

Figure 4. *FYCO1* (c.2206C>T) knock-in (KI) human embryonic stem cell (hESC)-derived lentoid bodies revealed opaque central zones. Phase-contrast microscopy was performed on differentiation days 25 and 35 during lentoid body formation. On differentiation day 25, *FYCO1* KI hESC-derived lentoid bodies show reduced transparency in the central zones compared with wild type (WT) hESC-derived lentoid bodies. The effect of the KI allele becomes more evident on day 35 with opaque zones present in the *FYCO1* KI hESC-derived lentoid bodies, in sharp contrast to the WT hESC-derived lentoid bodies that displayed extensive transparent zones. Note: Image magnification: 5x; Scale bars: 100 µm.

fiber-like cells (Figure 6) in the central portion of lentoid bodies. TEM revealed fewer cytoplasmic structures or organelles in both epithelial-like cells (Figure 5A, B, D, E) and fiber-like cells (Figure 6A, B, D, E) in WT hESC-derived lentoid bodies compared to *FYCO1* KI hESC-derived lentoid bodies. High-resolution TEM images confirmed the increased mass of ER (blue arrow), mitochondria (red arrow), and Golgi apparatus (GA; green arrow) in lens epithelial-like cells (Figure 5C, F) and fiber-like cells (Figure 6C, F) in *FYCO1* KI lentoid bodies compared to WT lentoid bodies.

TEM reveals retention of organelles in fyco1⁻/⁻ mice lenses at early postnatal time points

Although lentoid bodies mimic the ocular lens, they are not an absolute replica of the lens, in part, because they lack the surrounding tissues including the cornea and retina. We, therefore, performed TEM analysis of WT and *fyco1*⁻/⁻ mice lenses at P0 to identify changes in intracellular structure resulting from loss of FYCO1. The ultrastructural analysis of differentiating fiber cells in the transition zone of the WT P0 mice lenses revealed a few organelles i.e., mitochondria, GA, and ER (Figure 7A-B). In contrast to the P0 WT mice lenses, differentiating fiber cells in the transition zone of *fyco1*⁻/⁻ mice lenses showed retention of organelles including ER, GA, and mitochondria, suggesting impaired organelle removal (Figure 7C-D) compared to age-matched WT mice lenses.

We next completed TEM analysis of WT and *fyco1*⁻/⁻ mice lenses at P7, and P14 and consistent with the TEM results of P0 lenses, we observed retention of organelles in *fyco1*⁻/⁻ mice lenses at P7 (Fig. S4) and P14 (Fig. S5). These data are in agreement with the increased mass of organelles seen in the TEM analysis of *FYCO1* KI lentoid bodies (Figures 5-6).

Western blot analysis reveals increased intracellular organelle mass in fyco1⁻/⁻ mice lenses at early postnatal time points

The TEM analysis of *fyco1*⁻/⁻ mice lenses revealed retention of organelles in *fyco1*⁻/⁻ mice lenses. We next performed Western blot analysis to validate the increased organelle mass in *fyco1*⁻/⁻ mice lenses. We used HSPA5/BiP, an ER marker, to quantify the ER mass in *fyco1*⁻/⁻ mice lenses at P0, P7, P14, and P21. Western blot analysis revealed an increased ER mass in *fyco1*⁻/⁻ mice lenses at P0, P7, P14, and P21, respectively, compared to age-matched WT mice lenses (Fig. S6A-B), suggesting retention of ER in *fyco1*⁻/⁻ mice lenses. We further examined PDIA4/ERp72, another ER marker, and GOLGA1/Golgin-97, a GA marker to quantitate levels of ER and GA in *fyco1*⁻/⁻ mice lenses. The analysis suggested a higher mass of ER and GA in *fyco1*⁻/⁻ mice lenses at P7, and P14 compared to age-matched WT mice lenses (Fig. S6C-F) consistent with results shown in figures S4-5. These data also suggest that the difference in the concentration of organelles in WT and *fyco1*⁻/⁻ mice lenses decreases as the lenses age.
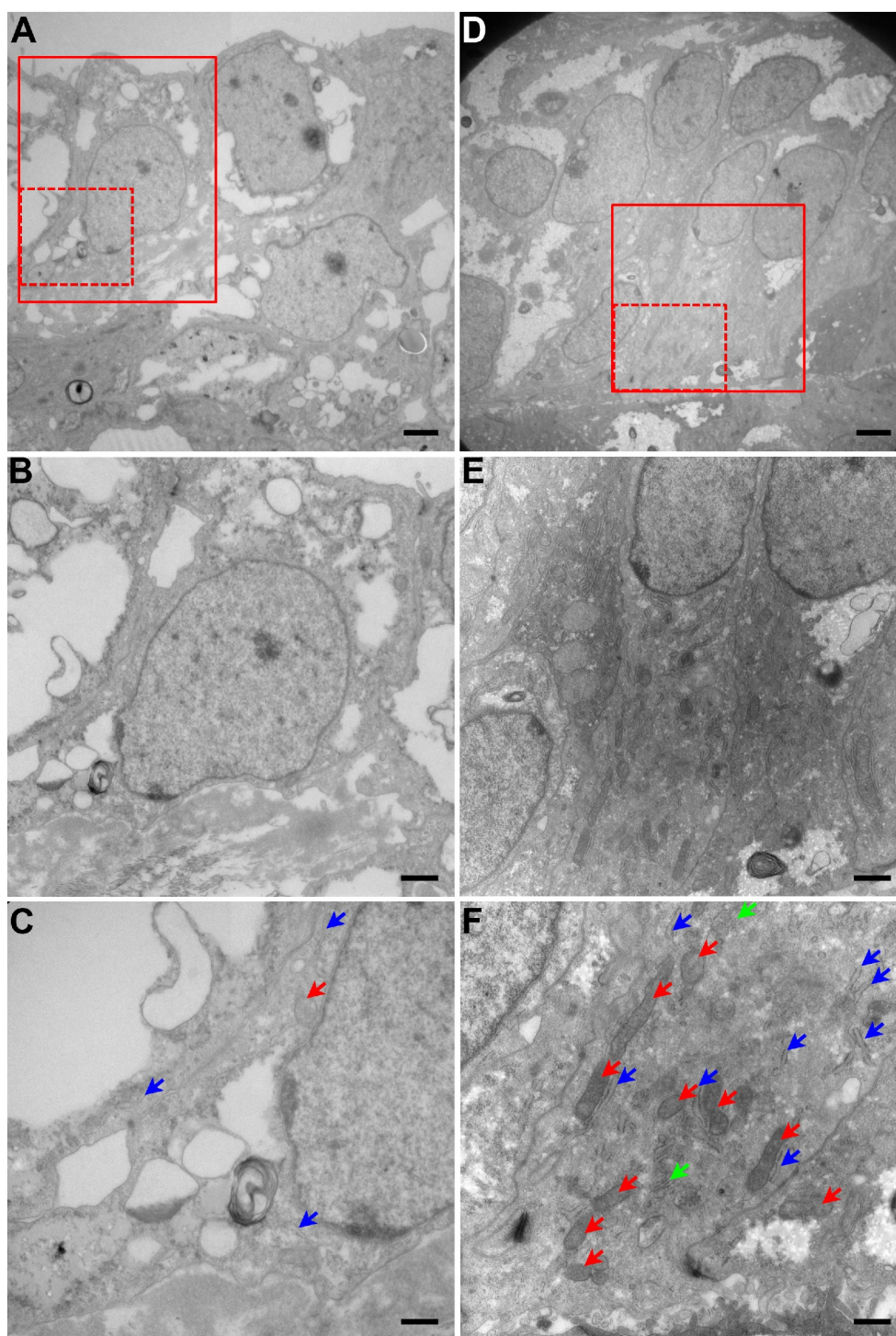
Figure 5. Transmission electron microscopy (TEM) of lens epithelial-like cells revealed retention of cellular organelles in *FYCO1* (c.2206C>T) knock-in (KI) human embryonic stem cell (hESC)-derived lentoid bodies on differentiation day 25. (A–C) Wild type (WT) lentoid bodies show relatively fewer endoplasmic reticulum (ER; blue arrow), Golgi apparatus (GA; green arrow), and mitochondria (red arrow), in lens epithelial-like cells. (D–F) In contrast to WT, lens epithelial-like cells in *FYCO1* KI hESC-derived lentoid bodies revealed an increased mass of ER, mitochondria, and GA. Note: Image magnifications: 6,000x (A, D), 12,000x (B, E), and 25,000x (C, F); Scale bars: 2 μm (A, D), 1 μm (B, E) and 500 nm (C, F). Panels B and C and panels E and F are enlarged images of the boxed areas (B and E: solid lines; C and F: broken lines) in panels A and D, respectively.

Discussion

We previously reported multiple mutant alleles of *FYCO1* responsible for arCC [19,20]. Here, we used *FYCO1* as an entry point to investigate the role of autophagy in lens morphogenesis using multiple approaches including a knockout mouse model, CRISPR-Cas9-engineered KI HLE cells, and KI H9 hESC-derived lentoid bodies. The *fyco1*$^{-/-}$ mice recapitulated the cataract phenotype and the
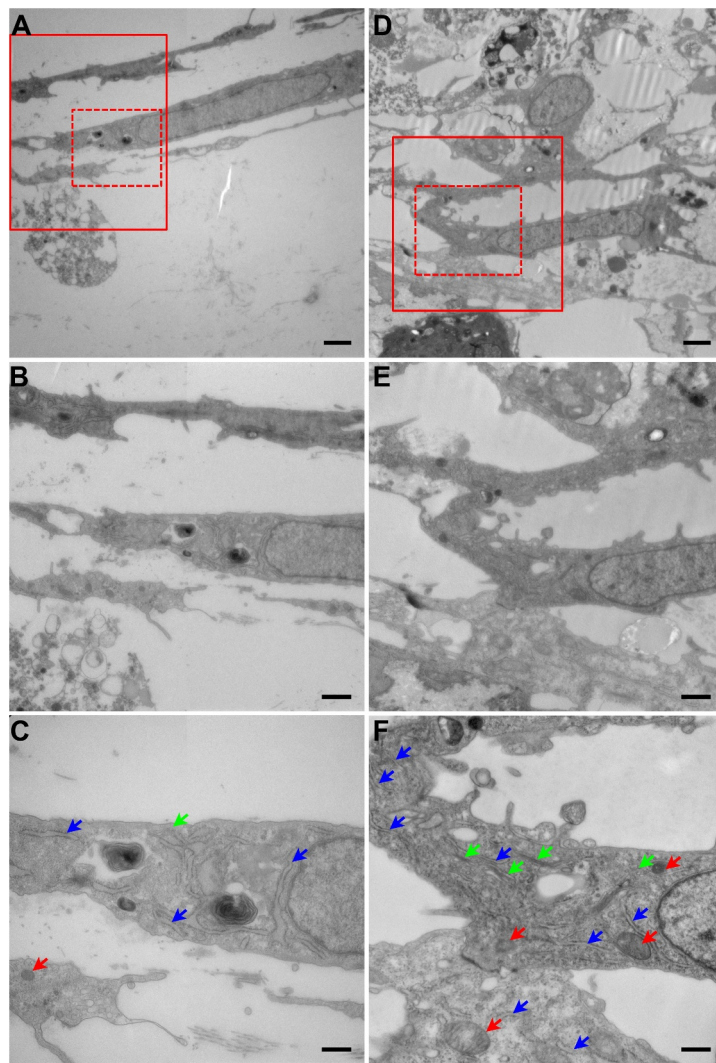
Figure 6. Transmission electron microscopy (TEM) of lens fiber-like cells revealed retention of cellular organelles in *FYCO1* (c.2206C>T) knock-in (KI) human embryonic stem cell (hESC)-derived lentoid bodies on differentiation day 25. (A–C) Wild type (WT) lentoid bodies show relatively fewer endoplasmic reticulum (ER; blue arrow), Golgi apparatus (GA; green arrow), and mitochondria (red arrow) in fiber-like cells. (D–F) In contrast to WT, *FYCO1* KI hESC-derived lentoid bodies revealed an increased mass of ER, mitochondria, and GA. Note: Image magnifications: 6,000x (A, D), 12,000x (B, E), and 25,000x (C, F); Scale bars: 2 μm (A, D), 1 μm (B, E) and 500 nm (C, F). Panels B and C and panels E and F are enlarged images of the boxed areas (B and E: solid lines; C and F: broken lines) in panels A and D, respectively.

transcriptome coupled with proteome and metabolome profiling identified many perturbed autophagy-related genes, proteins, and lipids, respectively suggestive of diminished autophagy in *fyco1*$^{-/-}$ mice lenses. The *FYCO1* KI HLE cells revealed a decrease in autophagic flux resulting from the loss of FYCO1 and TEM showed accumulation of organelles in *FYCO1* KI lentoid bodies and *fyco1*$^{-/-}$ mice lenses. Taken together, our data confirm the loss of FYCO1 results in a diminished autophagic flux, impaired organelle removal, and cataractogenesis.

The lens fiber cell differentiation and creation of the OFZ are complex processes with potentially multiple pathways essential for the transparency of the lens [4]. The role of autophagy in lens fiber cell differentiation is a topic of some controversy, with supporting data available for different viewpoints. There have been at least two reports where the authors based on their respective datasets have suggested that organelle removal during lens fiber cell differentiation is independent of autophagy [10,11]. In both these studies, the authors investigated the role of autophagy during lens fiber cell differentiation by examining the lenses of knock-out mice that were developed by the deletion of autophagy-related genes i.e., *Atg5* [10,11] and *Pik3c3/Vps34* [11]. The authors observed organelle degradation in the lens requires neither *Atg5*, nor *Pik3c3/Vps34*, and concluded that the organelle removal during lens fiber cell differentiation is independent of autophagy and that an autophagy-independent mechanism plays a primary role in the creation of the OFZ [10,11]. As also noted previously by Costello et al [14], neither of the two above-mentioned studies conclusively rule out the role of autophagy in organelle removal during lens fiber cell differentiation provided that autophagy can occur independently of *ATG5* [27] and *PIK3C3/VPS34* [28,29].

In contrast to the above-mentioned, there have been studies that support the role of autophagy in organelle removal during lens fiber cell differentiation. Basu et al reported the
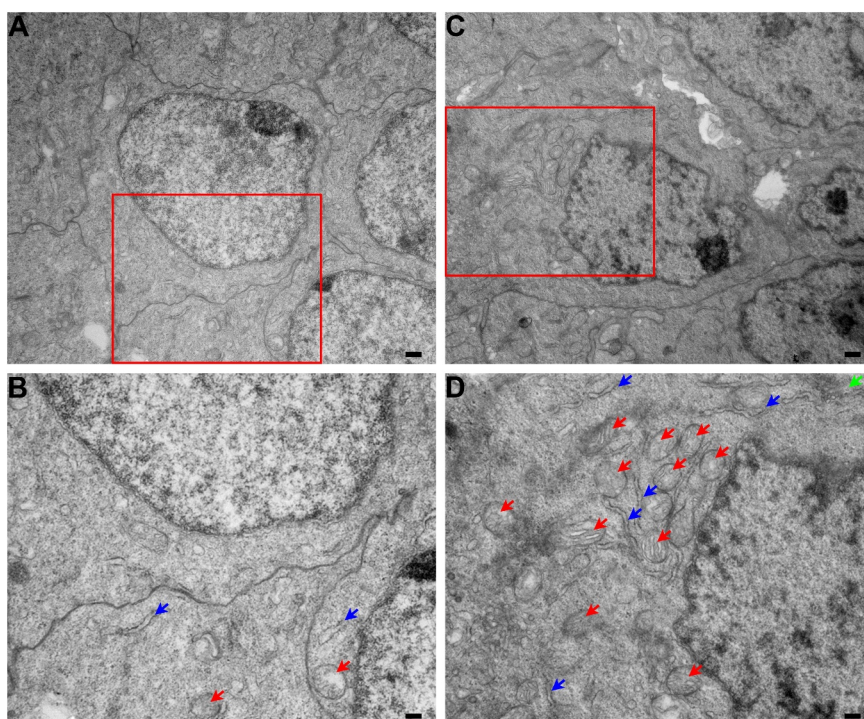
Figure 7. Transmission electron microscopy (TEM) of *fyco1* homozygous knockout (*fyco1*^{−/−}) mice lenses showed increased cellular organelles at postnatal day 0 (P0). (A, B) Wild type (WT) mice lenses at P0 exhibit differentiating fiber cells with few endoplasmic reticulum (ER; blue arrow), Golgi apparatus (GA; green arrow), and mitochondria (red arrow). (C,D) In contrast to WT, *fyco1*^{−/−} mice differentiating lens fiber cells showed retention of ER, mitochondria, and GA. Note: Image magnifications: 9700x (A, C), and 19,400x (B, D); Scale bars: 500 nm (A, C), and 250 nm (B, D). Panels B and D are enlarged images of the boxed areas in panels A and C, respectively.

role of autophagy in organelle removal especially in differentiating fiber cells [30]. The authors determined that suppression of MAPK/JNK-MTORC1 signaling leads to premature loss of organelles by autophagy during terminal differentiation of lens fiber cells [30]. Sidjanin et al showed that autophagosome maturation maintains lens transparency by mediating the removal of organelles from lens fiber cells [31]. The authors showed accumulation of SQSTM1/p62 in cortical and primary lens fiber cells in *tbc1d20* knockout mice [31], consistent with the higher level of SQSTM1/p62 in *fyco1*^{−/−} mice lenses. Costello et al identified mitochondria within autophagic vesicles in lens epithelial cells and early differentiating lens fiber cells through electron microscopy and dual-label confocal imaging [14]. Brennan et al showed retention of mitochondria, ER, and GA in differentiating fiber cells of *Bnip3l* knockout mice lenses [32]. *TDRD7*, a gene previously implicated in the pathogenies of cataracts and glaucoma [33], was recently reported to be involved in autophagosome maturation [34]. In the report, Tu et al established that loss of TDRD7 function results in eye defects and testicular abnormalities in mice, implicating autophagy in the lens morphogenesis and spermiogenesis [34].

Recently, two additional studies related to the role of autophagy in organelle removal during lens fiber cell differentiation were published [35,36]. In the first study by Ping et al, the authors used co-immunoprecipitation to show that GJA8 interacts with ATG16L1 and ATG12 [35]. The authors further determined that the number of autophagic vesicles was significantly decreased in lens fiber cells but not in epithelial cells in *gja8b* mutant zebrafish lenses [35] suggesting

that ablation of Gja8b results in downregulation of autophagy in lens fiber cells. Importantly, the authors demonstrated that downregulation of autophagy in lens fiber cells was accompanied by organelle degradation defects including retention of ER [35]. Intriguingly, the authors present convincing evidence that rapamycin treatment effectively relieved lens defects in *gja8b* mutant zebrafish, and the immunohistochemistry revealed that rapamycin treatment promoted organelle degradation, including loss of the ER and cytoskeleton in *gja8b* mutant zebrafish [35].

In the second study, Satoh et al reported that disrupting *Fyco1* in mice results in cataract formation accompanied by a decrease in LC3 conversion and accumulation of SQSTM1/p62 in lenses of *fyco1* knockout mice [36], consistent with the results shown in Figures 1–2. The authors further performed immunostaining of paraffin-embedded lenses from 12-week-old *fyco1* knockout mice and showed that nuclei, mitochondria, and ER were present in the cortical region but not in the OFZ [36]. Based on these immunostaining analyses, the authors suggest that FYCO1 is not required for organelle degradation in the OFZ [36]. While the results presented by Satoh et al show that the OFZ of 12-week-old *fyco1* knockout mice is devoid of nuclei, mitochondria and ER, these results do not rule out the role of autophagy in organelle removal during lens fiber cell differentiation at early postnatal time points.

To understand the role of FYCO1 in the lens, it is imperative to consider the genetic studies of *FYCO1* in patients with congenital cataracts [19,20]. In these studies, we reported 16 familial cases with multiple individuals in these families harboring loss-of-function mutations in *FYCO1*. All individuals

were examined thoroughly for both ocular and extra-ocular phenotypes and notably, none of the individuals homozygous for the loss-of-function mutations in *FYCO1* had any clinical diagnosis except bilateral cataracts. Given that autophagy is indispensable for the physiological functioning of many ocular and extra-ocular tissues including the retina and that FYCO1 is expressed in multiple tissues of the human body, these genetic data strongly suggest that loss of FYCO1 does not affect basal autophagy. If the loss of FYCO1 had affected the basal autophagy, individuals homozygous for null alleles (and *fyco1*$^{-/-}$ mice) would be expected to show many systemic anomalies since mutations affecting autophagy result in severe phenotypes [37,38].

We propose a model for the role of FYCO1-dependent autophagy in organelle removal during lens fiber cell differentiation, presented in Figure 8 based on the following: 1) the results of the human genetic studies where no phenotypes except bilateral cataracts have been identified in individuals homozygous for the loss-of-function mutations in *FYCO1*, 2) the reported role of FYCO1 to reside close to the membranes of the perinuclear ER, and binds to lipidated LC3 to deliver membranous structures to the sites of autophagosome formation [17], 3) the results shown in Figures 2-3 of loss of FYCO1-dependent decrease in autophagy and 4) the data presented in Figures 5-7 and figures S4-6 of impaired or delayed organelle removal. As shown in Figure 8, the baseline level of macroautophagy in the lens can occur independently of FYCO1, while FYCO1-dependent autophagy is required for cellular activities demanding high levels of autophagy, such as the removal of organelles during the creation of the OFZ. In baseline autophagy, as in any other cell type, organelles destined for degradation are sequestered by the expanding phagophore, leading to the formation of autophagosome. The autophagosome subsequently fuses with lysosomes, and the sequestered cargos are degraded or processed by hydrolases. FYCO1-dependent autophagy supplements basal autophagy in the lens by delivering pre-autophagosome membranes (Figure 8A), an established function of FYCO1 [17]. In the absence of FYCO1, the basal autophagy in the lens (of patients with loss-of-function mutations in *FYCO1* and *fyco1*$^{-/-}$ mice lenses) remains uninterrupted. However, the absence of FYCO1 results in a decrease in autophagosome formation to meet the physiological requirement of elevated levels of autophagy for organelle removal during the creation of the OFZ, which in turn, results in impaired organelle removal accompanied by altered expression of many proteases and cataractogenesis (Figure 8B).

Kuhn et al recently presented an analogous model in which FYCO1 is essential for adaptation to cardiac stress, and although the loss of FYCO1 does not affect basal autophagy
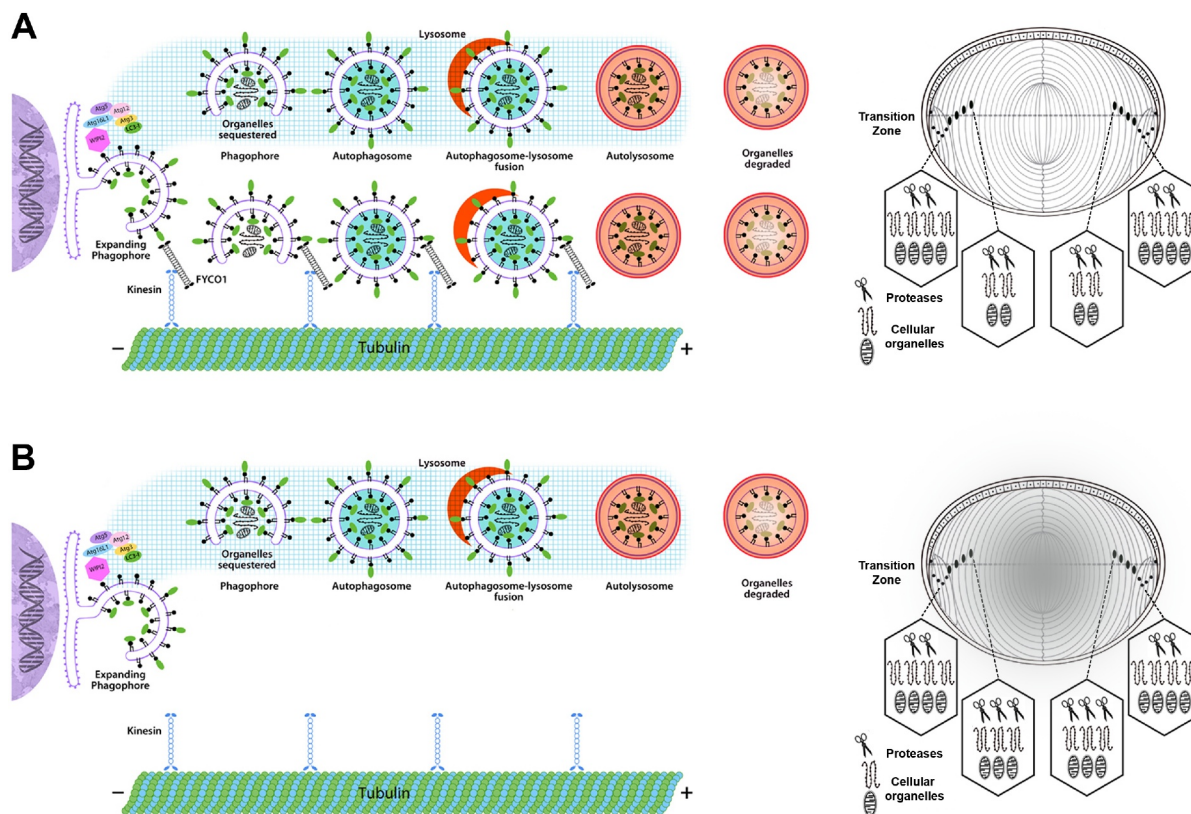

Figure 8. The proposed model for the role of FYCO1-dependent autophagy in organelle removal during lens fiber cell differentiation. (A) The baseline level of macroautophagy can occur independent of FYCO1, while FYCO1 helps with delivering extra autophagosome membranous structures to meet the physiological requirement of elevated levels of autophagy during creation of the organelle-free zone (OFZ). The cellular organelles are sequestered by the expanding phagophore, leading to the formation of the autophagosome. The autophagosome subsequently fuses with lysosomes, and the sequestered cargos are degraded or processed by hydrolases. (B) In the absence of FYCO1, the basal autophagy in the lens remains uninterrupted. However, the absence of FYCO1 results in a decrease in autophagosome formation to meet the physiological requirement of elevated levels of autophagy for organelle removal during the creation of the OFZ, which in turn, results in impaired organelle removal accompanied by altered expression of many proteases and cataractogenesis.

in isolated cardiomyocytes, it abolishes the induction of autophagy after glucose deprivation [39]. The authors further demonstrated that *fyco1*-deficient mice, when subjected to starvation, were unable to respond to induction of autophagy and developed impaired cardiac function [39]. A similar role of FYCO1 has been reported by Da et al in which RNP granule homeostasis in the chromatoid body is regulated by FYCO1-mediated autophagy [40]. The authors determined that induction of autophagy results in the recruitment of lysosomal vesicles onto the chromatoid body in FYCO1-dependent manner [40]. The authors observed that the cellular defects in *fyco1* conditional knockout mice germ cells were enhanced after challenging the cells in tubule culture conditions by autophagy inducers and inhibitors [40]. In light of their observations, the authors suggested that FYCO1-dependent processes are not required for spermatogenesis under physiological conditions but become critical when challenged by adverse conditions [40]. The results of the above-mentioned studies in two different tissues, i.e., heart and testis, are similar to the model shown in Figure 8 in which FYCO1 is needed to meet the physiological requirement for elevated levels of autophagy during lens fiber cell differentiation.

It is worth noting that our model does not suggest that autophagy is the sole cellular process responsible for organelle removal during lens fiber cell differentiation. Our model is in line with the concept that multiple, parallel and redundant pathways are involved in lens fiber cell differentiation and creation of the OFZ, and these pathways form interacting networks, and possibly these pathways can functionally compensate for each other [4]. Morishita et al recently reported organelle degradation by PLAAT (phospholipase A/acyltransferase)-family phospholipases in zebrafish and mice [41], which is in line with the notion that multiple pathways are essential for organelle removal during lens fiber cell differentiation and creation of the OFZ.

Finally, the question of whether the loss of FYCO1-dependent impaired organelle removal is directly responsible for cataracts or if cataractogenesis is a secondary effect remains unanswered. We observed altered expression of proteases in response to the loss of FYCO1-dependent decrease in autophagy, particularly CAPN3 (calpain 3), which showed nearly a two-fold increase in the *fyco1*$^{-/-}$ mice lens proteome (Table S2). Liu et al reported hyperactivation of calpain in the lens associated with fragmentation of critical lens proteins including SPTAN1/fodrin, BFSP1, VIM, TDRD7, and CAPRIN2 [42]. Since the loss of FYCO1 function only results in diminished autophagy and not a complete cessation, we speculate that it is not the impaired organelle removal directly but rather the increased expression of proteases in *fyco1*$^{-/-}$ mice lenses, perhaps as an attempt to compensate for the diminished levels of autophagy, that damages proteins essential for lens cell transparency and in turn result in cataracts. However, future studies examining the altered expression of proteases, and their respective substrates in *fyco1*$^{-/-}$ mice lenses will elucidate the role of proteases in the loss of FYCO1-dependent cataractogenesis.

Taken together, our data confirm an essential role of FYCO1-dependent autophagy in lens morphogenesis where FYCO1 is not required for basal autophagy but rather supplements autophagy for organelle removal during the creation of the OFZ. Importantly, these data strengthen the evidence supporting the notion that autophagy contributes to the removal of organelles during creation of the OFZ.

Materials and methods

Generation of fyco1$^{-/-}$ mice and examining the lens phenotype

A conditional knockout mouse with LoxP sites flanking exon 4 and 5 of *Fyco1* was obtained from Taconic Biosciences (Cologne, Germany). The *Fyco1* homozygous floxed LoxP male mice were crossed to C57BL/6 J female mice (The Jackson Laboratory, 000664). The *Fyco1* heterozygous floxed LoxP (*Fyco1*$^{+/-}$) mice were backcrossed to generate *Fyco1* homozygous floxed LoxP (*Fyco1*$^{+/+}$) mice. The *fyco1*$^{-/-}$ mice were generated by crossing *Fyco1*$^{+/+}$ mice with *EIIa*-Cre (The Jackson Laboratory, 003724), and *Prm1*-Cre (The Jackson Laboratory, 003328) transgenic mice. During the development of *fyco1*$^{-/-}$ mice and at regular intervals during the study, the genotype of mice were validated by examining the genomic DNA isolated from the tail of pups or mice. Briefly, mouse tail biopsies were digested overnight at 37°C with gentle shaking by adding 500 μl DNA digestion buffer (50 mM Tris-HCl, pH 8.0, 100 mM EDTA, pH 8.0, 1% SDS, 100 mM NaCl) with 0.5 mg/ml proteinase K (New England Biolabs Inc., P8107S). Approximately, 700 μl of phenol:chloroform:iso-amyl alcohol (25:24:1; MilliporeSigma, P3803) was added and mixed vigorously and centrifuged at 16,200 x g for 5 min, and the aqueous layer containing genomic DNA was collected into a microcentrifuge tube. Genomic DNA was precipitated with a one-tenth volume of 3 M sodium acetate, pH 5.2 (MilliporeSigma, S7899), and 2.5 volumes of 200 proof ethanol (Pharmco, 111000200) and pelleted by centrifugation at 16,200 x g for 5 min. The DNA pellets were washed with 70% cold ethanol and dissolved in TE buffer (MilliporeSigma, 93283).

Genomic DNA was PCR amplified to determine mice genotypes (WT, heterozygous, and homozygous) using forward (5′-GCGGTCTGGCAGTAAAAACTATC-3′) and reverse (5′-GTGAAACAGCATTGCTGTCACTT-3′) primers. The genotyping PCR reactions were completed in 10 μl reaction volume containing 20 ng of genomic DNA, 1 μl of each forward (10 μM) and reverse primer (10 μM), 1 μl of 10 x PCR buffer (100 mM Tris-HCl, pH 8.4, 400 mM NaCl, 15 mM MgCl$_2$, 2.5 mM spermidine [MilliporeSigma, S2626]), 250 μM dNTP mix (New England Biolabs Inc., N0447L), and 0.2 U of OneTaq DNA polymerase (New England Biolabs Inc., M0480L). PCR amplification consisted of an initial denaturation step at 95°C for 3 min followed by 35 cycles consisting of denaturation at 95°C for 30s, annealing at 52°C for 30s and elongation at 72°C for 60s, followed by a final elongation at 72°C for 2 min.

The expression of *Fyco1* (or lack thereof) in *fyco1*$^{-/-}$ mice lenses was determined by qRT-PCR. To extract the lenses, mice were anesthetized with isoflurane (MilliporeSigma, 26675–46-7) and euthanized through cervical dislocation.

The eyes were enucleated, and the lenses were isolated using forceps under a microscope. The lenses were dissolved in TRIzol reagent (Invitrogen, 15596026), and RNA was extracted as per the manufacturer's instructions. The quantity of the RNA was determined on a NanoDrop Lite Spectrophotometer (ThermoFisher Scientific) and was used to prepare first-strand cDNA using the Superscript III kit (Invitrogen, 18080051) as per the manufacturer's instructions. The qRT-PCR was performed on STEP ONE Real-Time PCR System (Applied Biosystems) using a pre-designed *Fyco1* TaqMan probe (Applied Biosystems, Mm00530503_m1). The Delta–delta C_T method was used to determine relative expression [43], with *Gapdh* TaqMan probe (Applied Biosystems, Mm99999915_g1) as an internal control to normalize the expression.

The opacities in the lens and the development of cataracts were examined at multiple postnatal time points. The eyes of age-matched WT and *fyco1*$^{-/-}$ mice were dilated using topical administration of 1% cyclopentolate (Bausch +Lomb Inc., NDC 24208–735-06) and 2.5% phenylephrine (Paragon BioTeck Inc., NDC 42702–102-15) solution. The mice were anesthetized by subcutaneous injection of ketamine-xylazine [100 mg/kg body weight for ketamine (MilliporeSigma, 1867–66-9) and 16 mg/kg body weight for xylazine (MilliporeSigma, 7361–61-7)] and cataracts were photographed by Micron III Imaging Microscope (Phoenix Research Labs).

Transcriptome profiling of fyco1$^{-/-}$ mice lenses

Next-generation RNA-Seq-based transcriptome profiling of WT and *fyco1*$^{-/-}$ mice lenses at P0 was performed to identify DE genes in *fyco1*$^{-/-}$ mice lenses. Three biological replicates of WT and *fyco1*$^{-/-}$ mice, each consisting of 10 lenses were used for RNA-Seq. The lenses of WT and *fyco1*$^{-/-}$ P0 mice were extracted as described above for generation of *fyco1*$^{-/-}$ mice. The lenses were frozen immediately after extraction at −80°C until further processing. RNA was extracted from WT and *fyco1*$^{-/-}$ mice lenses using TRIzol reagent (Invitrogen, 15596018) as per the manufacturer's instructions. The extracted RNA was examined by a NanoDrop Lite spectrophotometer and using the RNA 6000 Pico kit (Agilent, 5067–1513) on an Agilent 2100 Bioanalyzer (Agilent).

The RNA-Seq bar-coded library preparation, next-generation RNA-Seq, and raw data analysis were performed commercially by Novogene Inc. (Sacramento, CA). RNA-Seq raw reads and processed data have been deposited in the NCBI Gene Expression Omnibus and are accessible through the GEO accession number GSE143251.

The expression data were normalized by calculating the FPKM values for each gene [44]. Differential gene expression analysis was performed using the DESeq2 (Ver. 2_1.6.3) [45]. The statistical significance was estimated by a two-tailed, one-sample t-test statistical procedure, assuming a hypothesized mean of 0 change.

Proteome profiling of fyco1$^{-/-}$ mice lenses

Mass spectrometry-based proteome profiling of WT and *fyco1*$^{-/-}$ mice lenses at P0 was completed to identify proteins exhibiting differential concentrations (abundance or deficiency) in *fyco1*$^{-/-}$ mice lenses. Three biological replicates of WT and *fyco1*$^{-/-}$ mice lenses, each consisting of eight lenses were investigated in separate tandem mass tags (TMT) runs as described [46]. The lenses of WT and *fyco1*$^{-/-}$ P0 mice were extracted as described above for generation of *fyco1*$^{-/-}$ mice. The protein extraction, digestion, and labeling with TMT reagent, and mass spectrometry were performed as described [46]. The mass spectrometry data have been deposited to the ProteomeXchange Consortium via the PRIDE partner repository and are accessible through the dataset identifier PXD006381.

All three TMT runs were processed in a single Proteome Discoverer analysis using the TMT sets as replicates. The Proteome Discoverer summed all the reporter ion intensities of peptide spectrum matches (PSMs) for the corresponding proteins in each of the TMT runs, separately. After protein identification and quantification, the protein table was exported to Perseus software (ver. 1.5.2.6) for normalization of the reporter ion intensities [47]. The reporter ion intensities in each of the three replicates were divided by the reporter ion intensity of the WT mice lenses in each TMT set, separately. Finally, each column was divided by the median value of the corresponding column to remove systematic deviation as described [46].

The reporter ion intensities from each TMT set were imported into Partek Genomics Suite (Ver. 6.6; Partek Inc.) to examine proteins exhibiting differential concentrations in *fyco1*$^{-/-}$ mice lenses. The normalized reporter ion intensities (normalized against WT P0 mice lenses in each TMT set, independently) were examined for SD to identify proteins exhibiting higher levels (i.e., accumulated) and displaying lower levels (i.e., diminished) in *fyco1*$^{-/-}$ mice lenses. The statistical significance was estimated by a two-tailed, one-sample t-test statistical procedure, assuming a hypothesized mean of 0 change.

Metabolome profiling of fyco1$^{-/-}$ mice lenses

Mass spectrometry-based metabolome profiling of WT and *fyco1*$^{-/-}$ mice lenses at P0 was performed to identify metabolites exhibiting differential concentrations (abundance or deficiency) in *fyco1*$^{-/-}$ mice lenses. The lenses of WT and *fyco1*$^{-/-}$ P0 mice were extracted as described above for generation of *fyco1*$^{-/-}$ mice. Four biological replicates of WT and *fyco1*$^{-/-}$ mice, each consisting of 25 mg lens mass were used for metabolome profiling as described [48].

The sample preparation, mass spectrometry, and raw data analysis were completed commercially by Metabolon, Inc. (Morrisville, NC). Data extraction, quantification of peaks, and quality control were performed as described [49,50]. The metabolome data of WT and *fyco1*$^{-/-}$ mice

lenses have been deposited in the MetaboLights repository and are accessible through the study identifier MTBLS206.

The data of each sample was normalized to account for differences in metabolite levels due to differences in the amount of material present in each sample. The ArrayStudio, R programs (http://cran.r-project.org/) and JMP (https://www.jmp.com) was used for statistical analyses. After normalization and imputation of missing values, if any, Welch's two-sample t-test was used to identify metabolites that exhibited a significant differential in $fyco1^{-/-}$ mice lenses.

TEM of P60 fyco1 $^{-/-}$ mice lenses

The lenses of WT and $fyco1^{-/-}$ P60 mice were extracted as described above for generation of $fyco1^{-/-}$ mice and were immediately fixed in freshly prepared primary fixative solution (2% paraformaldehyde, 2% glutaraldehyde, 0.08 M PO_4, 3 mM $MgCl_2$, pH 7.2) overnight at 4°C. Samples were then rinsed in cold 100 mM maleate buffer, pH 6.2 containing 3% sucrose (336 mOsmols; MilliporeSigma, M9009) for 30 min and en-bloc stained with filtered 2% uranyl acetate in maleate containing sucrose, in the dark at 4°C. Culture dishes were then dehydrated at 4°C up to 70% ethanol, transferred to room temperature, and further dehydrated to 100% ethanol. Plates were then infiltrated with pure resin (PolyBed 812; Polysciences, 08792) and cured for three days at 37°C, and one day at 60°C. Hardened blocks were removed from the plastic plates and the blocks were trimmed and sectioned. Sections (80nm) were cut on a Reichert Ultracut E microtome with a Diatome diamond knife (45 degrees), were picked up on formvar-coated 1×2 mm copper slot grids (EMS, FF 2010-Cu) and stained with methanolic uranyl acetate followed by lead citrate. Grids were viewed on a Hitachi H 7600 TEM operating at 80 kV and digital images were captured with an XR50 CCD camera by Advanced Microscopy Techniques (Woburn, MA).

Western blot analysis of SQSTM1/p62 at P0

The Western blot analysis was performed using WT and $fyco1^{-/-}$ mice lenses to examine SQSTM1/p62 at P0. Three biological replicates of WT and $fyco1^{-/-}$ mice, each consisting of 10 pups were used for Western blot analysis. The lenses of WT and $fyco1^{-/-}$ P0 mice were extracted as described above for generation of $fyco1^{-/-}$ mice and were immediately stored at −80°C until further use for protein extraction and Western blot analysis.

The Western blot was performed using an automated capillary electrophoresis immunoassay machine (WES ProteinSimple), commercially. Each sample consisting of 0.2 mg/ml of total protein was used for capillary electrophoresis. Proteins were separated based on their respective size and probed by the SQSTM1/p62 antibody (R&D Systems; MAB8028). An anti-Mouse Detection Module (ProteinSimple, DM-002) was employed for detection of the target protein and creation of a digitized Western blot image. The intensity of each sample was normalized using the ACTB/β-actin antibody (MilliporeSigma, A5441).

Multiphoton laser-scanning imaging of fyco1$^{-/-}$ mice lenses

The CAG-RFP-EGFP-Map1lc3b transgenic mice (The Jackson Laboratory, 027139) were bred with $fyco1^{-/-}$ mice to generate a transgenic line expressing RFP-EGFP-MAP1LC3B. The CAG-RFP-EGFP-Map1lc3b WT and CAG-RFP-EGFP -Map1lc3b-fyco1$^{-/-}$ mice lenses were examined under a multiphoton laser-scanning microscope (Olympus, FV1000MPE) with LUMPLFLN 40x water-immersion, 0.8 numerical-aperture objective lenses. The WT and $fyco1^{-/-}$ mice lenses expressing RFP-EGFP-MAP1LC3B were extracted as described above for generation of $fyco1^{-/-}$ mice and were immediately fixed in 3.7% paraformaldehyde (MilliporeSigma, P62148) overnight at 4°C. Lenses were placed on agarose gel with the anterior side of the lens facing the objective. Multiple lens images were collected at an increment of 10 μm (Z-stacks) using three fluorescent channels (blue, green, and red). Mean RFP and GFP fluorescence intensities of the first five stacks (anterior lens including lens epithelium) and the combination of all stacks (whole lens) were quantitated using Fiji software (https://imagej.net/software/fiji/).

CRISPR-Cas9-mediated genome editing to generate FYCO1 KI HLE cells

HLE cells (HLE-B3; ATCC, CRL-11421) were cultured in Eagle's Minimum Essential Medium (EMEM; ATCC, 30–2003) supplemented with 20% fetal bovine serum (Sigma, F6178), 100 IU/ml penicillin-100 μg/ml streptomycin solution (MilliporeSigma, P0781) and 2.5 μg/ml amphotericin B (MilliporeSigma, A2942) in a 5% CO_2 incubator at 37°C.

The HLE cells harboring the cataract causing mutation in FYCO1 (c.2206C>T; p.Q736*) were engineered using the CRISPR-Cas9 genome editing methodology. A guide RNA (gRNA) targeting the genomic sequence in FYCO1 (i.e., c.2206C) was cloned into a GFP-CRISPR-Cas9 vector commercially (ATUM, pD1401-AD). The plasmid was transformed into Stbl3 competent cells (Invitrogen, C737303) and endotoxin-free plasmid DNA was purified using the Endo-Free Plasmid Maxi Kit (QIAGEN,12362). In parallel, genomic DNA of a patient homozygous for the FYCO1 (c.2206C>T) allele was amplified through PCR using a forward primer (5`-AGCAGGCCAGC ATCCGGCACTTGG-3`) and reverse primer (5`-TGCAGCCGTTGGACCTCCCCCTGA-3`) to prepare the donor DNA.

Transfection was performed in a large Nucleocuvette (Lonza, V4XC-1012). HLE cells were grown to nearly 70% confluency and approximately 3×10^6 cells, cell count determined using an automated cell counter (Countess; Invitrogen), were pelleted by centrifugation at 100 g for 3 min. The pelleted cells were resuspended in 100 μl of SE buffer (Lonza, V4XC-1012) and supplement solution containing 7.5 μg of plasmid DNA harboring the gRNA, and 5.8 μg of double-stranded donor DNA. The 100 μl mixture was gently transferred to a large Nucleocuvette, and the transfection was performed as per manufacturer's instructions using a pre-optimized Nucleofector program (Lonza).

Subsequently, 500 µl of pre-warmed EMEM medium was added to the Nucleocuvette and transferred to a T-75 culture flask. The medium was changed 6 h post-transfection and single cells expressing GFP were sorted into 96-well plates 24 h post-transfection using FACS Aria IIu Sorter (BD Biosciences).

The 96-well plates were examined under the microscope 24 h post-sorting to validate that each well had a single cell and the wells with more than one cell were discarded. The single cells in the selected wells were grown and upon being confluent, a portion of the colony was removed from each well, and the genomic DNA was extracted from harvested cells. The genomic DNA was examined to confirm the presence of the *FYCO1* (c.2206C>T) allele through bi-directional Sanger sequencing.

WT and *FYCO1* KI HLE cells were harvested to evaluate the endogenous expression of *FYCO1* mRNA. Total RNA was isolated by TRIzol reagent, and the quality of the total RNA was determined on a NanoDrop Lite Spectrophotometer. The first-strand cDNA synthesis was completed using the Superscript III kit as per the manufacturer's instructions. The qRT-PCR was performed on STEP ONE Real-Time PCR System (Applied Biosystems) using a pre-designed *FYCO1* TaqMan probe (Applied Biosystems, Hs00225888_m1). The Delta–delta C_T method was used to determine relative expression [43], with *ACTB* TaqMan probe (Applied Biosystems, Hs01060665_g1) as an internal control to normalize the expression.

shRNA-mediated knockdown of FYCO1 in HLE cells

A cocktail of four pre-designed shRNAs in a lentiviral GFP vector targeting *FYCO1* was purchased (OriGene, TL304437) along with scrambled shRNA (OriGene, TR30021). The plasmids were transformed into Stbl3 competent cells (Invitrogen, C737303) and endotoxin-free plasmid DNA was purified using the EndoFree Plasmid Maxi Kit.

Transfections were performed in triplicate for both *FYCO1* and scrambled shRNA (used as a control) in a 16-well Nucleocuvette strip (Lonza, V4XC-1032). HLE cells were grown to nearly 70% confluency approximately 3×10^5 cells, cell count determined using an automated cell counter, were pelleted by centrifugation at 100 g for 3 min and resuspended in a 20 µl SE solution (Lonza, V4XC-1032). A total of 1 µg plasmid DNA (combining 250 ng DNA from each of the four shRNAs) targeting *FYCO1* or 1 µg of the scrambled shRNA was used for single transfection. Transfection was performed as per manufacturer's instructions using a pre-optimized Nucleofector program (Lonza).

After transfection, cells were immediately resuspended in a pre-warmed EMEM medium and were gently transferred to a 100 mm cell culture petri dish. The medium was changed 6 h post-transfection and transfected cells were harvested 48 h post-transfection for RNA isolation followed by cDNA synthesis as described above for the *FYCO1* KI HLE cells. The expression of *FYCO1* in transfected cells was examined by a TaqMan assay as described above for the *FYCO1* KI HLE cells.

Functional analysis of FYCO1 KI HLE cells

The quantification of endogenous SQSTM1/p62 protein in *FYCO1* KI HLE cells was completed by antibody-based flow cytometry. Briefly, WT and *FYCO1* KI HLE cells were washed with 1 x PBS (ThermoFisher Scientific, 10010023), fixed with 1% paraformaldehyde at 4°C for 15 min, and permeabilized with 0.5% PBST (0.5% Tween-20 [MilliporeSigma, P9416] in 1 x PBS) at 4°C for 15 min. Next, the permeabilized cells were incubated with SQSTM1/p62 mouse monoclonal antibody (1:100 dilution; Abcam, ab56416) and mouse IgG2a isotype control (ThermoFisher Scientific, MA1-10419) at 4°C for 1 h. Next, the cells were washed one time with 0.1% PBST (0.1% Tween-20 in 1 x PBS) and incubated with FITC-conjugated anti-mouse secondary antibody (1:50 dilution; Santa Cruz Biotechnology, sc-2099) at 4°C for 40 min. Finally, cells were washed with 0.1% PBST and fixed with 1% paraformaldehyde. Cells (10,000 per sample) were analyzed using a guava easyCyte flow cytometer (EMD Millipore) and data were analyzed by guavaSoft (guavaSoft v3.1.1; EMD Millipore).

The autophagic flux in *FYCO1* KI HLE cells was measured by the relative fluorescence of MAP1LC3B-tagged mRFP and GFP in *FYCO1* KI HLE cells. Briefly, WT and *FYCO1* KI HLE cells were transfected with mRFP-GFP-LC3 plasmid (21074; Addgene; deposited by Tamotsu Yoshimori) as described above for generation of *FYCO1* KI HLE cells. The transfected cells were treated with 500 nM rapamycin (MilliporeSigma, R8781), an autophagy inducer, and two lysosomal protease inhibitors, E64d (10 µg/ml; MilliporeSigma, E8640) and pepstatin A (10 µg/ml; MilliporeSigma, P5318) 24 h post-transfection for 4 h. The treated cells washed with ice-cold 1 x PBS and resuspended in ice-cold 1 x PBS containing 0.05% bovine serum albumin (BSA; MilliporeSigma, A-9647). The cells (10,000 per sample) were analyzed using a guava easyCyte flow cytometer (EMD Millipore) and the red and green fluorescence intensities were calculated for WT and *FYCO1* KI HLE cells (guavaSoft, Ver. 3.1.1; EMD Millipore).

The quantification of LC3B-II in *FYCO1* KI HLE cells was examined by relative fluorescence of MAP1LC3B-tagged GFP in *FYCO1* KI HLE cells. Briefly, WT and *FYCO1* KI HLE cells were transfected with an EGFP-LC3B plasmid (Plasmid 11546; Addgene; deposited by Karla Kirkegaard) as described above for generation of *FYCO1* KI HLE cells. The transfected cells were treated with 50 µM chloroquine (MilliporeSigma, C6628) 24 h post-transfection for 4 h and the cells were harvested in a 15 ml polypropylene conical tube followed by a single wash with ice-cold 1 x PBS. Next, cells were treated with freshly prepared 0.05% saponin (MilliporeSigma, SAE0073) in 1 x PBS for 30s. After saponin treatment, the cells were washed with 1 x PBS and resuspended in ice-cold 1 x PBS containing 0.05% BSA. The resuspended samples were transferred into 5 ml polypropylene FACS tubes (Falcon, 352063) and kept on ice until further analysis. 30,000 cells per sample were analyzed using the LSR II flow cytometer (Becton Dickinson). The mean GFP fluorescence intensity was calculated for each sample by FlowJo (Ver. 10; Tree

Star, Inc Ashland, OR). The mean GFP fluorescence intensity of WT HLE cells was set to 100% to compare and normalize the mean GFP fluorescence intensity of *FYCO1* KI HLE cells.

The autophagic flux in WT and *FYCO1* KI HLE cells was examined through the detection of autophagic vacuoles using the CYTO-ID autophagy detection kit (Enzo Life Sciences, ENZ-51031-K200). Briefly, WT and *FYCO1* KI HLE cells were treated with 50 µM chloroquine (MilliporeSigma, C6628) for 4 h and harvested in a 15 ml polypropylene conical tube. The chloroquine treated cells were washed with 1 x assay buffer and resuspended in 250 µl of CYTO-ID followed by incubation at 37°C for 30 min as per the manufacturer's instructions. Finally, the CYTO-ID-stained cells were washed one time with 1 x assay buffer and resuspended in 300 µl of 1 x assay buffer supplemented with 0.05% BSA. 30,000 cells per sample were analyzed using the guava easyCyte flow cytometer for data acquisition and analysis (guavaSoft, Ver. 3.1.1; EMD Millipore). The mean fluorescence intensity was calculated for each sample. The mean fluorescence intensity of WT HLE cells was set to 100% to compare and normalize the GFP MFI in *FYCO1* KI HLE cells.

CRISPR-Cas9-mediated genome editing to generate FYCO1 KI hESCs

The H9 hESCs (WiCell Research Institute, WA09) were cultured in mTeSR1 medium (StemCell Technologies, 85850) in feeder-free conditions on Matrigel (Corning, 354277) coated plates in a 5% CO_2 incubator at 37°C. The culture medium was changed each day and the cells were passaged using 0.5 mM EDTA in 1 x PBS every 4–5 days.

The hESC harboring the cataract causing mutation in *FYCO1* (c.2206C>T; p.Q736*) was developed through CRISPR-Cas9 genome editing as described above for KI HLE cells. The plasmid containing the gRNA, targeting the genomic sequence in *FYCO1* (i.e., c.2206C) and the donor DNA homozygous for *FYCO1* (c.2206C>T) allele were prepared as described above for developing the KI HLE cells. The FuGene 6 reagent (Promega, E2691) was used for transfection of hESCs according to the manufacturer's instructions. The hESCs were grown for 3–4 passages in mTeSR1 medium for transfection. Upon 70–80% confluence, the mTeSR1 medium was removed and the colonies were washed twice with DMEM/F12 (ThermoFisher Scientific, 11330032), dissociated into single cells by accutase (MilliporeSigma, A6964), replated at 750,000 cells per well in a 6-well plate, and transfected 4–5 h later.

The FuGene 6 reagent (10.5 ul) added to 50 µl of Opti-MEM (ThermoFisher Scientific, 31985062) was mixed with a DNA mixture (1.5 µg of plasmid DNA harboring the gRNA, Cas9 and GFP, and 2 µg double-stranded donor DNA in 50 µl of Opti-MEM) in a 3:1 ratio and placed at room temperature for 15 min. The FuGene 6 transfection Reagent-DNA mixture was added to a well containing the single hESC colony seeded in 2 ml fresh mTeSR1 medium. The plate was gently shaken and placed in an incubator and the mTeSR1 medium was replaced 12 h post-transfection. The transfected hESCs were sorted based on GFP 48 h post-transfection using FACS Aria

IIu Sorter and plated in a 6-well plate at low density. A portion of the single hESC clones was picked to confirm the presence of *FYCO1* (c.2206C>T) allele through bi-directional Sanger sequencing. The clones positive for the *FYCO1* (c.2206C>T) allele were subcloned to establish single cell clonality. The *FYCO1* KI hESCs were evaluated for endogenous expression of *FYCO1* mRNA as described for *FYCO1* KI HLE cells.

Differentiation of FYCO1 KI hESCs to lentoid bodies

H9 hESCs were differentiated into lentoid bodies using the "fried-egg" method published initially by Fu et al [24] and later by Ali et al [25,26] with a few modifications. Briefly, 60–70 H9 hESC colonies with roughly 25 cells in each colony were cultured in mTeSR1 medium on a Matrigel-coated, 35-mm culture plate. The differentiating hESCs were treated with 100 ng/ml of Noggin (a BMP [bone morphogenetic protein] inhibitor; R&D Systems, 6997-NG-025) 4 h post-plating, which continued for six days (day 0 to day 6).

On day 6, 60–65 differentiating hESCs along with surrounding epithelial-like cells were mechanically detached and reseeded in Matrigel-coated 35-mm plates containing a cocktail of 100 ng/ml of FGF2/bFGF (fibroblast growth factor 2; R&D Systems, 233-FB-025), 20 ng/ml BMP4 (bone morphogenetic protein 4; R&D Systems, 314-BP-010), and 20 ng/ml BMP7 (bone morphogenetic protein 7; R&D Systems, 354-BP-010) for nine days (day 6 to day 15). On day 11, cell clusters that did not form "fried egg" morphologies were mechanically removed while the cells clusters forming the "fried egg" morphologies were further treated with 100 ng/ml of FGF2, 20 ng/ml BMP4, and 20 ng/ml BMP7 until day 15. On day 15, cell clusters were treated with 20 ng/ml WNT3A (Peprotech, 315–20) along with 100 ng/ml FGF2 to differentiate lens epithelial-like cells into lens fiber-like cells until the lentoid bodies were harvested i.e., day 25.

Phase-contrast microscopy was performed at multiple time points during the differentiation process using a Zeiss microscope (Zeiss) equipped with Q-Capture camera (QImaging Inc) at 5x, 10x, 20x, and 40x magnifications.

Proteome profiling of FYCO1 KI hESC-derived lentoid bodies

The proteome of WT hESC- and *FYCO1* KI hESC-derived lentoid bodies on differentiation day 25 was examined through mass-spectrometry-based TMT proteome profiling as described [26,46]. A total of five WT hESC- and *FYCO1* KI hESC-derived whole lentoid bodies on differentiation day 25 were harvested and pooled as one biological replicate. Three biological replicates of WT hESC- and *FYCO1* KI-derived lentoid bodies were examined in the 6-plex TMT experiment to identify proteins exhibiting differential concentrations (abundance or deficiency) in *FYCO1* KI lentoid bodies.

A total of 400 µg of each sample was processed for protein isolation and digestion as described [26]. The peptides were separated by basic pH reversed-phase liquid chromatography

(bRPLC) into 96 fractions followed by concatenation into 24 fractions as described [26]. The labeling with TMT reagents, liquid chromatography, and mass spectrometry was performed on a ThermoFisher instrument as described [46]. The mass spectrometry data of *FYCO1* KI hESC-derived lentoid bodies have been deposited to the ProteomeXchange Consortium via the PRIDE partner repository and are accessible through the dataset identifier PXD017001.

The reporter ion intensities were imported into Partek Genomics Suite (Ver. 6.6; Partek Inc.) to investigate proteins exhibiting differential concentrations in *FYCO1* KI hESC-derived lentoid bodies. The normalized reporter ion intensities were examined for the SD to identify proteins exhibiting higher (i.e., accumulated) or lower levels (i.e., diminished) in *FYCO1* KI hESC-derived lentoid body proteome. The statistical significance was estimated by a two-tailed one-sample t-test statistical procedure, assuming a hypothesized mean of 0 change.

TEM of FYCO1 *KI hESC-derived lentoid bodies*

The WT hESC- and *FYCO1* KI hESC-derived lentoid bodies on differentiation day 25 were harvested and immediately rinsed with 1x PBS for 30s, followed by treatment with a mixture of 2.5 ml of 2.5% glutaraldehyde in 0.1 M phosphate (Sorenson's) and 5 mM $MgCl_2$ buffer (pH 7.4) for 4 h with slow rocking at room temperature. Subsequently, lentoid bodies were fixed with 1% OsO_4 (EMS, 19190) in 0.1 M phosphate buffer (pH 7.4; Baker, Monobasic 3818, Dibasic 3824) for 2 h with slow rocking at 4°C. The remaining steps including sample processing, sectioning, and imaging are the same as described above for P60 WT and *fyco1*$^{-/-}$ mice lenses.

TEM of developing fyco1$^{-/-}$ *mice lenses*

The WT and *fyco1*$^{-/-}$ mice lenses at P0, P7, and P14 were extracted as described above for generation of *fyco1*$^{-/-}$ mice. The extracted lenses were subjected to sample preparation including fixation, sectioning, staining, and imaging for TEM as described above for P60 WT and *fyco1*$^{-/-}$ mice lenses.

Western blot of fyco1$^{-/-}$ *mice lenses*

WT and *fyco1*$^{-/-}$ mice lenses were extracted as described above for generation of *fyco1*$^{-/-}$ mice at four time points (P0, P7, P14, and P21) and lens fiber cells were subjected to Western blot analysis. An equal amount of protein (~400 μg) was electrophoresed in 10% SDS-PAGE gel in 1x running buffer (25 mM Tris, 190 mM Glycine, 0.1% SDS) using a Bio-Rad Mini-Protean II system (Bio-Rad). After electrophoresis, the proteins were transferred from the PAGE gel to a nitrocellulose membrane (0.45 μm; ThermoFisher Scientific, LC2003) using a Blot transfer system (Bio-Rad). Subsequent to the transfer, the membranes were rinsed twice with 1x TBST buffer (20 mM Tris-HCl, pH 7.4, 0.137 M NaCl, 0.1% Tween 20) and blocked in 5% nonfat dry milk (Bio-Rad, 1706404) in 1x TBST for 20 min at room temperature, followed by incubation with anti-rabbit monoclonal primary antibodies; HSPA5/BiP (1:1000; Cell Signaling Technology,

3177) in 5% nonfat dried milk in TBST overnight at 4°C. After the primary antibody treatment, membranes were washed three times in 1x TBST and incubated with an anti-rabbit immunoglobulin IgG, HRP-linked secondary antibody (1:1000; Cell Signaling Technology, 7074) for 1 h at room temperature. After the secondary antibody treatment, the membranes were washed five times with 1x TBST, and incubated for 5 min in SuperSignal West Dura Extended Duration Substrate (ThermoFisher Scientific, 34075). The blots were visualized using a ChemiDoc XRS+ system (Bio-Rad) and densitometry analysis was performed using Image Lab software (Bio-Rad). Equal loading was determined by the quantification of ACTB/β-actin (Cell Signaling Technology, 4967).

The capillary electrophoresis-based Western blot analysis was performed using PDIA4/ERp72 (Cell Signaling Technology, 5033) and GOLGA1/Golgin-97 (Cell Signaling Technology, 13192) as described above for SQSTM1/p62.

Statistical analyses

The statistical significance was estimated by a one- or two-tailed, t-test. The estimate of the spread within a dataset was measured by calculating SD of three or more replicates of each experiment.

Disclosure statement

No potential conflict of interest was reported by the author(s).

References

[1] Jean D, Ewan K, Gruss P. Molecular regulators involved in vertebrate eye development. Mech Dev. 1998;76(1–2):3–18.

[2] McAvoy JW, Chamberlain CG, de Iongh RU, et al. Lens development. Eye (Lond). 1999;13(Pt 3b):425–437.

[3] Bassnett S, Mataic D. Chromatin degradation in differentiating fiber cells of the eye lens. J Cell Biol. 1997;137(1):37–49.

[4] Wride MA. Lens fibre cell differentiation and organelle loss: many paths lead to clarity. Philos Trans R Soc Lond B Biol Sci. 2011;366 (1568):1219–1233.

[5] Zandy AJ, Bassnett S. Proteolytic mechanisms underlying mitochondrial degradation in the ocular lens. Invest Ophthalmol Vis Sci. 2007;48(1):293–302.

[6] Pendergrass W, Penn P, Possin D, et al. Accumulation of DNA, nuclear and mitochondrial debris, and ROS at sites of age-related cortical cataract in mice. Invest Ophthalmol Vis Sci. 2005;46 (12):4661–4670.

[7] Pendergrass W, Zitnik G, Urfer SR, et al. Age-related retention of fiber cell nuclei and nuclear fragments in the lens cortices of multiple species. Mol Vis. 2011;17:2672–2684.

[8] Shiels A, Hejtmancik JF. Biology of inherited cataracts and opportunities for treatment. Annu Rev Vis Sci. 2019;5:123–149.

[9] Frost LS, Mitchell CH, Boesze-Battaglia K. Autophagy in the eye: implications for ocular cell health. Exp Eye Res. 2014;124:56–66.

[10] Matsui M, Yamamoto A, Kuma A, et al. Organelle degradation during the lens and erythroid differentiation is independent of autophagy. Biochem Biophys Res Commun. 2006;339(2):485–489.

[11] Morishita H, Eguchi S, Kimura H, et al. Deletion of autophagy-related 5 (Atg5) and Pik3c3 genes in the lens causes cataract independent of programmed organelle degradation. J Biol Chem. 2013;288(16):11436–11447.

[12] Brennan LA, Kantorow WL, Chauss D, et al. Spatial expression patterns of autophagy genes in the eye lens and induction of autophagy in lens cells. Mol Vis. 2012;18:1773–1786.

[13] Khan SY, Hackett SF, Lee M-CW, et al. Transcriptome profiling of developing murine lens through RNA sequencing. Invest Ophthalmol Vis Sci. 2015;56(8):4919–4926.

[14] Costello MJ, Brennan LA, Basu S, et al. Autophagy and mitophagy participate in ocular lens organelle degradation. Exp Eye Res. 2013;116:141–150.

[15] Mizushima N, Yamamoto A, Matsui M, et al. In vivo analysis of autophagy in response to nutrient starvation using transgenic mice expressing a fluorescent autophagosome marker. Mol Biol Cell. 2004;15(3):1101–1111.

[16] Gaullier JM, Simonsen A, D'Arrigo A, et al. FYVE fingers bind PtdIns(3)P. Nature. 1998;394(6692):432–433.

[17] Pankiv S, Alemu EA, Brech A, et al. FYCO1 is a Rab7 effector that binds to LC3 and PI3P to mediate microtubule plus end-directed vesicle transport. J Cell Biol. 2010;188(2):253–269.

[18] Cheng X, Wang Y, Gong Y, et al. Structural basis of FYCO1 and MAP1LC3A interaction reveals a novel binding mode for Atg8-family proteins. Autophagy. 2016;12(8):1330–1339.

[19] Chen J, Ma Z, Jiao X, et al. Mutations in FYCO1 cause autosomal-recessive congenital cataracts. Am J Hum Genet. 2011;88(6):827–838.

[20] Iqbal H, Khan SY, Zhou L, et al. Mutations in FYCO1 identified in families with congenital cataracts. Mol Vis. 2020;26:334–344.

[21] Schuiki I, Schnabl M, Czabany T, et al. Phosphatidylethanolamine synthesized by four different pathways is supplied to the plasma membrane of the yeast Saccharomyces cerevisiae. Biochim Biophys Acta. 2010;1801(4):480–486.

[22] Kochl R, Hu XW, Chan EY, et al. Microtubules facilitate autophagosome formation and fusion of autophagosomes with endosomes. Traffic. 2006;7(2):129–145.

[23] Eng KE, Panas MD, Karlsson Hedestam GB, et al. A novel quantitative flow cytometry-based assay for autophagy. Autophagy. 2010;6(5):634–641.

[24] Fu Q, Qin Z, Jin X, et al. Generation of functional lentoid bodies from human induced pluripotent stem cells derived from urinary cells. Invest Ophthalmol Vis Sci. 2017;58(1):517–527.

[25] Ali M, Kabir F, Thomson JJ, et al. Comparative transcriptome analysis of hESC- and iPSC-derived lentoid bodies. Sci Rep. 2019;9(1):18552.

[26] Ali M, Kabir F, Raskar S, et al. Generation and proteome profiling of PBMC-originated, iPSC-derived lentoid bodies. Stem Cell Res. 2020;46:101813.

[27] Nishida Y, Arakawa S, Fujitani K, et al. Discovery of Atg5/Atg7-independent alternative macroautophagy. Nature. 2009;461(7264):654–658.

[28] Martens S, Rusten TE, Kraft C. Autophagy at sea. Autophagy. 2013;9(9):1286–1291.

[29] Zhou X, Wang L, Hasegawa H, et al. Deletion of PIK3C3/Vps34 in sensory neurons causes rapid neurodegeneration by disrupting the endosomal but not the autophagic pathway. Proc Natl Acad Sci U S A. 2010;107(20):9424–9429.

[30] Basu S, Rajakaruna S, Reyes B, et al. Suppression of MAPK/JNK-MTORC1 signaling leads to premature loss of organelles and nuclei by autophagy during terminal differentiation of lens fiber cells. Autophagy. 2014;10(7):1193–1211.

[31] Sidjanin DJ, Park AK, Ronchetti A, et al. TBC1D20 mediates autophagy as a key regulator of autophagosome maturation. Autophagy. 2016;12(10):1759–1775.

[32] Brennan LA, McGreal-Estrada R, Logan CM, et al. BNIP3L/NIX is required for elimination of mitochondria, endoplasmic reticulum and Golgi apparatus during eye lens organelle-free zone formation. Exp Eye Res. 2018;174:173–184.

[33] Lachke SA, Alkuraya FS, Kneeland SC, et al. Mutations in the RNA granule component TDRD7 cause cataract and glaucoma. Science. 2011;331(6024):1571–1576.

[34] Tu C, Li H, and Liu X, et al. TDRD7 participates in lens development and spermiogenesis by mediating autophagosome maturation. Autophagy. 2021;17(11):3848–3864.

[35] Ping X, Liang J, and Shi K, et al. Rapamycin relieves the cataract caused by ablation of Gja8b through stimulating autophagy in zebrafish. Autophagy. 2021;17(11):3323–333.

[36] Satoh K, Takemura Y, Satoh M, et al. Loss of FYCO1 leads to cataract formation. Sci Rep. 2021;11(1):13771.

[37] Levine B, Kroemer G. Biological functions of autophagy genes: a disease perspective. Cell. 2019;176(1–2):11–42.

[38] Mizushima N, Levine B. Autophagy in human diseases. N Engl J Med. 2020;383(16):1564–1576.

[39] Kuhn C, Menke M, Senger F, et al. FYCO1 regulates cardiomyocyte autophagy and prevents heart failure due to pressure overload in vivo. JACC Basic Transl Sci. 2021;6(4):365–380.

[40] Da RM, Lehtiniemi T, Olotu O, et al. FYCO1 and autophagy control the integrity of the haploid male germ cell-specific RNP granules. Autophagy. 2017;13(2):302–321.

[41] Morishita H, Eguchi T, Tsukamoto S, et al. Organelle degradation in the lens by PLAAT phospholipases. Nature. 2021;592(7855):634–638.

[42] Liu K, Lyu L, Chin D, et al. Altered ubiquitin causes perturbed calcium homeostasis, hyperactivation of calpain, dysregulated differentiation, and cataract. Proc Natl Acad Sci U S A. 2015;112(4):1071–1076.

[43] Livak KJ, Schmittgen TD. Analysis of relative gene expression data using real-time quantitative PCR and the 2(-Delta Delta C (T)) method. Methods. 2001;25(4):402–408.

[44] Mortazavi A, Williams BA, McCue K, et al. Mapping and quantifying mammalian transcriptomes by RNA-Seq. Nat Methods. 2008;5(7):621–628.

[45] Anders S, Huber W. Differential expression analysis for sequence count data. Genome Biol. 2010;11(10):R106.

[46] Khan SY, Ali M, Kabir F, et al. Proteome profiling of developing murine lens through mass spectrometry. Invest Ophthalmol Vis Sci. 2018;59(1):100–107.

[47] Tyanova S, Temu T, Sinitcyn P, et al. The Perseus computational platform for comprehensive analysis of (prote)omics data. Nat Methods. 2016;13(9):731–740.

[48] Khan SY, Ali M, and Riazuddin SA. Metabolome profiling of the developing murine lens. Experimental Eye Research. 2021;108343.

[49] Evans AM, DeHaven CD, Barrett T, et al. Integrated, nontargeted ultrahigh performance liquid chromatography/electrospray ionization tandem mass spectrometry platform for the identification and relative quantification of the small-molecule complement of biological systems. Anal Chem. 2009;81(16):6656–6667.

[50] DeHaven CD, Evans AM, Dai H, et al. Organization of GC/MS and LC/MS metabolomics data into chemical libraries. J Cheminform. 2010;2(1):9.